University of New Mexico
UNM Digital Repository

Chemical and Biological Engineering ETDs | Engineering ETDs

6-25-2010

Atomic-level investigation of surface processes governing SiGe wetting layer formation using STM/STS

Kyle J. Solis

Follow this and additional works at: https://digitalrepository.unm.edu/cbe_etds

Recommended Citation

Solis, Kyle J.. "Atomic-level investigation of surface processes governing SiGe wetting layer formation using STM/STS." (2010). https://digitalrepository.unm.edu/cbe_etds/33

This Thesis is brought to you for free and open access by the Engineering ETDs at UNM Digital Repository. It has been accepted for inclusion in Chemical and Biological Engineering ETDs by an authorized administrator of UNM Digital Repository. For more information, please contact disc@unm.edu.

Kyle J. Solis
Candidate

Chemical and Nuclear Engineering
Department

This thesis is approved, and it is acceptable in quality and form for publication:

Approved by the Thesis Committee:

Prof. Sang M. Han , Chairperson

Dr. Brian S. Swartzentruber 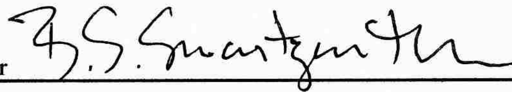

Prof. Ganesh Balakrishnan 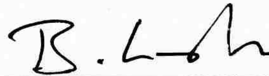

ATOMIC-LEVEL INVESTIGATION OF SURFACE PROCESSES GOVERNING SIGE WETTING LAYER FORMATION USING STM/STS

BY

KYLE J. SOLIS

B.S., UNIVERSITY OF NEW MEXICO, 2003

THESIS

Submitted in Partial Fulfillment of the
Requirements for the Degree of

Master of Science
Chemical Engineering

The University of New Mexico
Albuquerque, New Mexico

May, 2010

©2010, Kyle J. Solis

DEDICATION

To My Parents, Bobbie and Joey.

ACKNOWLEDGEMENTS

The author gratefully appreciates:

Sang M. Han for acquiring and providing research funding, and his mentorship in developing my skills in experimentation and writing, and for his overall support;

Brian S. Swartzentruber at Sandia National Laboratories* for his generosity with STM resources and his expertise, mentorship and overall support;

Lance R. Williams for his programming expertise in developing the image analysis algorithm used in this work;

Ganesh Balakrishnan for valuable comments and serving on my Thesis committee;

My family and friends for their loving support and endless patience!

Funding for the work of this Thesis was provided by:

National Science Foundation CAREER (DMR-0094145)

U.S. Army Research Laboratory and

U.S. Army Research Office (W911NF-05-1-0012)

*Sandia National Laboratories is a multi-program laboratory operated by Sandia Corporation, a wholly owned subsidiary of Lockheed Martin company, for the U.S. Department of Energy's National Nuclear Security Administration under contract DE-AC04-94AL85000.

ATOMIC-LEVEL INVESTIGATION OF SURFACE PROCESSES GOVERNING SIGE WETTING LAYER FORMATION USING STM/STS

BY

KYLE J. SOLIS

ABSTRACT OF THESIS

Submitted in Partial Fulfillment of the
Requirements for the Degree of

Master of Science
Chemical Engineering

The University of New Mexico
Albuquerque, New Mexico

May, 2010

ATOMIC-LEVEL INVESTIGATION OF SURFACE PROCESSES GOVERNING SIGE WETTING LAYER FORMATION USING STM/STS

by

Kyle J. Solis

B.S., Chemical Engineering, University of New Mexico, 2003
M.S., Chemical Engineering, University of New Mexico, 2010

ABSTRACT

Upon sub-monolayer Ge deposition on the $2\times n$ reconstructed SiGe alloy wetting layer at room temperature, the predominant adspecies observed are so-called *addimer chain structures* (ADCSs). Polarity-switching scanning tunneling microscopy (STM) is used to study ADCSs, as they only appear in empty-state images. ADCSs are dilute structures comprising type-C addimers that reside in neighboring troughs and extend along all equivalent ⟨130⟩ directions of the surface, giving rise to a zigzagged morphology. ADCSs exhibit localized movements, wherein their rearrangements are strongly coupled with the structure of the underlying substrate dimers. At elevated temperatures, ADCSs are observed to transition to compact epitaxial segments of the next atomic layer, indicating their metastability. By measuring ADCS transition rates over the temperature range of 90–150°C, an activation energy of 0.7 ± 0.2 eV and an associated prefactor of $5 \times 10^{4\pm2}$ s^{-1} are computed. Both of these kinetic values are quite low as compared to typical surface diffusion phenomena, and we suggest that the transition mechanism is likely complex and multi-bodied, requiring concerted rearrangements of the addimer chain with underlying substrate dimers.

To achieve chemical contrast between Si and Ge in the alloy wetting layer, preliminary investigations using scanning tunneling spectroscopy were conducted. A variety of surfaces with

increasing Ge compositions were investigated. It is shown that for low Ge compositions of about 0.1 monolayers (ML) or below, low-bias empty-state STM imaging is useful in determining the locations of Ge intermixing. At higher compositions (0.25–0.5 ML), considerable contrast and structure in the conductance images is observed that corresponds to structure in STM images and the Ge content of the surface. For compositions of 1.5 ML, which give rise to a fully-developed $2\times n$ reconstruction, the only structure in conductance images corresponds to the locations of the dimer vacancy lines, perhaps indicating sub-surface Ge depletion zones.

TABLE OF CONTENTS

LIST OF FIGURES ... **xi**

Chapter 1 Introduction ... **1**

1.1 References ... 4

Chapter 2 Experimental techniques, setup, and procedures ... **7**

2.1 Molecular Beam Epitaxy ... 7

2.2 Scanning Tunneling Microscopy ... 9

2.2.1 General description ... 9

2.2.2 STM Theory ... 10

2.3 Tunneling spectroscopy with the STM ... 13

2.3.1 General description ... 13

2.3.2 Structure and physics of semiconductors ... 14

2.3.3 Tunneling spectroscopy techniques ... 17

Voltage dependent spectroscopy ... 17

Scanning tunneling spectroscopy ... 18

2.4 Experimental setup and generalized procedure ... 19

Experimental setup ... 19

Generalized experimental procedure ... 20

2.5 References ... 21

Chapter 3 Polarity-switching scanning tunneling microscopy of addimer chain structures ... **23**

3.1 Heteroepitaxy of Ge on Si(001)–(2×1) ... 23

3.2 Heteroepitaxy of Ge on Ge-Si(001)–(2×n) ... 28

3.3 Formation of ADCSs ... 31
3.4 Mobility of ADCSs ... 34
3.5 Kink-to-straight ratio of ADCSs ... 37
3.6 Transition of ADCSs to compact epitaxial islands ... 40
3.7 Conclusions ... 44
3.8 References ... 45
Chapter 4 Scanning tunneling spectroscopy of the SiGe alloy wetting layer ... 50
4.1 Si(001)–(2×1) surface ... 51
4.2 $Si_{1-x}Ge_x$ alloy wetting layer ... 57
4.3 Conclusions ... 71
4.4 References ... 73
Chapter 5 Conclusions and future directions ... 76
5.1 References ... 79
Appendix Image processing algorithm ... 80

LIST OF FIGURES

Figure 1-1. Scanning tunneling microscope image of a clean SiGe alloy surface exhibiting 2×*n* reconstruction 3

Figure 2-1. Schematic of MBE and surface processes of adspecies 8

Figure 2-2. Illustration of the concept of tunneling 11

Figure 2-3. Schematics illustrating the STM process 12

Figure 2-4. Semiconductor band formation energy level diagram........ 15

Figure 2-5. Schematics of the DOS and Fermi-Dirac distribution function 16

Figure 2-6. Schematics illustrating STS concepts........ 18

Figure 3-1 STM images showing the morphological evolution with increasing Ge exposure on Si(001) 25

Figure 3-2. Various addimer adsorption sites, orientations, and nomenclature for a (2×1) surface 27

Figure 3-3. Sub-ML Ge coverage on Si(001) 28

Figure 3-4. STM images (200 Å × 200 Å) of the 2×*n* reconstructed SiGe wetting layer after sub-ML Ge deposition. 29

Figure 3-5. Schematic illustrating the relative positions of the constituent C-dimers (gold) of an ADCS in relation to substrate dimers........ 30

Figure 3-6. Monomer binding sites........ 32

Figure 3-7. Adatom-Trapping-Addition mechanism 33

Figure 3-8. Orientation and nomenclature for ADCS constituent addimers........ 34

Figure 3-9. ADCS-induced phase shift in buckling registry of surface dimers. 36

Figure 3-10. Schematic illustrating the number of unique configurations for a five-unit ADCS 38

Figure 3-11. Schematic illustrating configurational ordering of unbuckled substrate dimers (red) in relation to the ADCS orientation kinks vs. straight (gold). 39

Figure 3-12. Filled- and empty-state STM images showing an ADCS before and after its transition to a compact island. 41

Figure 3-13. Typical temporal ADCS population decay data with associated time constant 42

Figure 3-14. Arrhenius plot for 90°C < T < 150°C showing activation energy and pre-exponential factor associated with ADCS-island transition 43

Figure 4-1. Si(001)-(2×1) surface 52

Figure 4-2. Physical and electronic structure of Si(001)–(2×1) reconstruction 53

Figure 4-3. Commonly observed surface defects on Si(001)–(2×1) 54

Figure 4-4. Three common surface reconstructions for Si(001) 55

Figure 4-5. STS of Si(001)–(2×1). 56

Figure 4-6. Buckling and charge transfer in mixed SiGe dimers 59

Figure 4-7. Effect of the applied bias magnitude on the resolution of Ge intermixing sites in empty-state STM images 60

Figure 4-8. SiGe surface with 0.04 ML Ge deposited 61

Figure 4-9. Filled- and empty-state STM images of a SiGe surface at 0.10 ML Ge exposure. 62

Figure 4-10. SiGe surface at 0.25 ML of Ge 63

Figure 4-11. SiGe surface at 0.25 ML of Ge 64

Figure 4-12. SiGe surface at 0.25 ML of Ge.. 65

Figure 4-13. SiGe surface at 0.25 ML of Ge.. 66

Figure 4-14. Dimer vacancy lines indicating onset of the $2\times n$ reconstruction
in SiGe alloy.. 67

Figure 4-15. SiGe surface at 0.5 ML of Ge.. 68

Figure 4-16. SiGe surface at 0.5 ML of Ge.. 69

Figure 4-17. SiGe surface at 1.5 ML of Ge.. 70

Figure A-1. Original empty-state STM image 81

Figure A-2. Processed empty-state STM image... 82

Chapter 1

Introduction

Silicon-Germanium (SiGe), is a technologically-important [1–3] alloy of the Group IV semiconductors silicon and germanium. While both elements bond in the diamond cubic crystal structure, a lattice mismatch of 4.2% gives rise to a considerable amount of strain at the interface between these materials. This misfit strain manifests itself structurally and electronically, ultimately influencing device performance. Some of the positive effects of strain include an increase in charge carrier mobility [4–6], nanostructure formation [7–9], and band gap alteration [10–12]. However, strain also can cause an increase in the density of defects and dislocations, adversely affecting device performance [13].

It is the above-mentioned positive effects of strain that have driven SiGe to become an increasingly important material for many device applications [3]. For instance, SiGe is an excellent material choice for graded buffer layers [14–17] to integrate III-V materials to silicon substrates [18], as its lattice parameter can be tuned by manipulating the composition of the SiGe alloy $Si_{1-x}Ge_x$ $(0 \leq x \leq 1)$ in accord with Vegard's law. The desire for ever-increasing-speed microprocessors demands high-speed transistors, which has been traditionally dominated by III-V compound semiconductors. However, SiGe/strained Si technology is becoming competitive, with 500 GHz heterojunction bipolar transistors [19–21]. SiGe heterostructures are also finding application in optoelectronics as modulators, photodetectors, and light emitters [3,22–25]. Finally, SiGe is becoming a popular material for use in photovoltaics applications, such as multijunction solar cells [26–28]. The key advantage of SiGe in regards to these applications is the ease with which SiGe technology can be integrated into the current Si CMOS processing infrastructure [29].

Thus, the remaining engineering challenge is to take advantage of the numerous potential benefits of the SiGe heterosystem, which are *de facto* strain related, while mitigating the *undesirable* strain effects.

An essential step toward fully enabling and developing SiGe with many of the aforementioned technologies, relies on the ability to *selectively* grow high-quality (low-defect-density) Ge on Si, in addition to precise control over size and spatial distributions at the nanoscale. Indeed, if Ge is haphazardly grown on Si, a preponderance of defects will populate the grown Ge film due to the misfit strain. However, the observation of selective growth of Ge on Si over SiO_2 has been exploited to grow high-quality Ge films on Si(001) [30–32]. To better understand such selectivity and controllability, we study the surface processes responsible for heteroepitaxial film growth of Ge on Si(001) at the atomic level using scanning tunneling microscopy (STM). Our interests include identification of the main mass transport species; their interactions with other adspecies and the surface; and the relative stabilities of the various surface adspecies and adstructures. Herein, we specifically focus on the kinetics of compact epitaxial island formation on the Ge–Si(001)-($2\times n$) alloyed wetting layer, and the structure of the wetting layer itself.

The heteroepitaxy of Ge on Si(001) is a model example of the Stranski–Krastanov growth mode, in which a pseudomorphic two-dimensional wetting layer is initially formed, followed by the nucleation and growth of three-dimensional islands. Upon ~1.5 monolayers of Ge exposure, a clean Si(001)–(2×1) surface is first transformed into an alloyed SiGe wetting layer, exhibiting a $2\times n$ reconstruction as shown in Figure 1. For this particular reconstruction, every n^{th} dimer is missing from the surface, forming long-range ordered dimer vacancy lines that extend perpendicular to the substrate dimer rows. These vacancy lines decrease misfit stress by allowing the compressed substrate dimers to relax outwards.

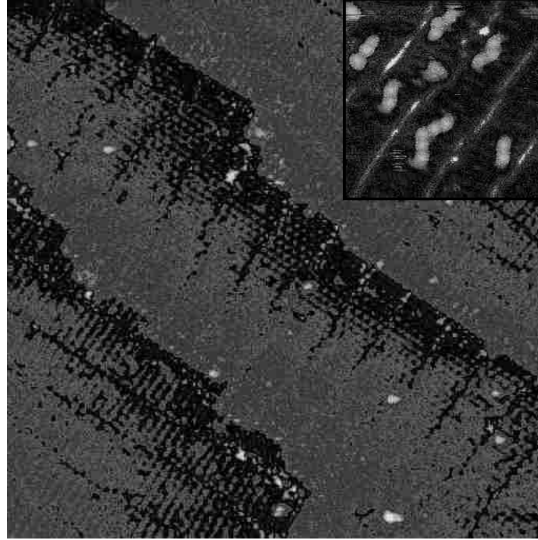

Figure 1-1. Scanning tunneling microscope image of a clean SiGe alloy surface exhibiting 2×*n* reconstruction. Dimer vacancy lines are seen to extend across the surface at ~45°. (Scan area is 250 Å × 250 Å). Inset shows a different 2×*n* surface with ADCSs appearing as chains of white dots.

Upon sub-monolayer Ge deposition on the SiGe alloy surface at room temperature, we have discovered the predominant mass transport species to be *addimer chain structures* (ADCSs). These structures, seen as the white features in the inset, only appear under certain imaging conditions with STM. At elevated temperatures (~90 °C), we observe the transition of these chain structures into compact epitaxial islands, which are segments of the next growth layer. This transition indicates that ADCSs are metastable precursors during epitaxial growth on the alloy surface whose formation is dominated by kinetics. The purpose of this Thesis is to characterize the mobility, configurational energetics, and activation energy associated with the transition of these metastable ADCSs to compact islands, in addition to investigating the electronic structure of the SiGe wetting layer to achieve chemical contrast between Si and Ge. Hopefully the information contained herein is helpful toward establishing a better understanding of the early stages of epitaxial growth of this technologically-important material.

1.1 *References*

[1] J. Ouellette, Silicon-Germanium Gives Semiconductors the Edge in *The Industrial Physicist* p.22 (American Institute of Physics) June/July 2002.

[2] M. Horn-von Hoegen, *Surf. Sci.* **537**, 1 (2003).

[3] D.J. Paul, *Semicond. Sci. Technol.* **19**, R75 (2004).

[4] K. Ismail, M. Arafa, K.L. Saenger, J.O. Chu, and B.S. Meyerson, *Appl. Phys. Lett.* **66**, 1077 (1995).

[5] R.J.P. Lander, Y.V. Ponomarev, J.G.M. van Berkum, and W.B. de Boer, *IEEE Trans. Electron Dev.* **48**, 1826 (2001).

[6] M.T. Currie, C.W. Leitz, T.A. Langdo, G. Taraschi, and E.A. Fitzgerald, *J. Vac. Sci. Technol. B* **19**, 2268 (2001).

[7] D.J. Eaglesham and M. Cerullo, *Phys. Rev. Lett.* **64**, 1943 (1990).

[8] Y.-W. Mo, D.E. Savage, B.S. Swartzentruber, and M.G. Lagally, *Phys. Rev. Lett.* **65**, 1020 (1990).

[9] O.P. Pchelyakov, Yu.B. Bolkhovityanov, A.V. Dvurechenskiĭ, L.V. Sokolov, A.I. Nikiforov, A.I. Yakimov, and B. Voigtländer, *Semiconductors* **34**, 1229 (2000).

[10] K.L. Wang, S.G. Thomas, and M.O. Tanner, *J. Mater. Sci.-Mater. El.* **6**, 311 (1995).

[11] Y.-S. Chieh, J.P. Krusius, D. Green, and M. Öztürk, *IEEE Electron Dev. Lett.* **17**, 360 (1996).

[12] M. Yoshimi, M. Terauchi, A. Nishiyama, O. Arisumi, A. Murakoshi, K. Matsuzawa, N. Shigyo, S. Takeno, M. Tomita, K. Suzuki, Y. Ushiku, and H. Tango, *IEEE Trans. Electron Dev.* **44**, 423 (1997).

[13] E.A. Fitzgerald, S.B. Samavedam, Y.H. Xie, and L.M. Giovane, *J. Vac. Sci. Technol. A* **15**, 1048 (1997).

[14] E.A. Fitzgerald, Y.-H. Xie, M.L. Green, D. Brasen, A.R. Kortan, J. Michel, Y.-J. Mii, and B.E. Weir, *Appl. Phys. Lett.* **59**, 811 (1991).

[15] F. Schäffler, D. Többen, H.-J. Herzog, G. Abstreiter, and B. Holländer, *Semicond. Sci. Technol.* **7**, 260 (1992).

[16] F.K. LeGoues, B.S. Meyerson, J.F. Morar, and P.D. Kirchner, *J. Appl. Phys.* **71**, 4230 (1992).

[17] T.H. Loh, H.S. Nguyen, C.H. Tung, A.D. Trigg, G.Q. Lo, N. Balasubramanian, D.L. Kwong, and S. Tripathy, *Appl. Phys. Lett.* **90**, 092108 (2007).

[18] E.A. Fitzgerald, Y.-H. Xie, D. Monroe, P.J. Silverman, J.M. Kuo, A.R. Kortan, F.A. Thiel, and B.E. Weir, *J. Vac. Sci. Technol. B* **10**, 1807 (1992).

[19] R. Krithivasan, Y. Lu, J.D. Cressler, J.-S. Rieh, M.H. Khater, D. Ahlgren, and G. Freeman, *IEEE Electron Dev. Lett.* **27**, 567 (2006).

[20] N. Zerounian, F. Aniel, B. Barbalat, P. Chevalier, and A. Chantre, *Electron. Lett.* **43**, 774 (2007).

[21] J. Yuan, J.D. Cressler, R. Krithivasan, T. Thrivikraman, M.H. Khater, D.C. Ahlgren, A.J. Joseph, and J.-S. Rieh, *IEEE Trans. Electron Dev.* **56**, 1007 (2009).

[22] T.P. Pearsall, *Mat. Sci. Eng. B* **9**, 225 (1991).

[23] B. Schüppert, J. Schmidtchen, A. Splett, U. Fischer, T. Zinke, R. Moosburger, and K. Petermann, *J. Lightwave Technol.* **14**, 2311 (1996).

[24] M. Stoffel, U. Denker, G.S. Kar, H. Sigg, and O.G. Schmidt, *Appl. Phys. Lett.* **83**, 2910 (2003).

[25] V.A. Egorov, G.É. Cirlin, A.A. Tonkikh, V.G. Talalaev, A.G. Makarov, N.N. Ledentsov, V.M. Ustinov, N.D. Zakharov, and P. Werner, *Phys. Solid State* **46**, 49 (2004).

[26] J. Yang, A. Banerjee, and S. Guha, *Appl. Phys. Lett.* **70**, 2975 (1997).

[27] X. Deng, X. Liao, S. Han, H. Povolny, and P. Agarwal, *Sol. Energ. Mat. Sol. C* **62**, 89 (2000).

[28] G. Sun, F. Chang, and R.A. Soref, *Opt. Express* **18**, 3746 (2010).

[29] D.J. Paul, *Adv. Mater.* **11**, 191 (1999).

[30] Q. Li, S.M. Han, S.R.J. Brueck, S. Hersee, Y.-B. Jiang, and H. Xu, *Appl. Phys. Lett.* **83**, 5032 (2003).

[31] Q. Li, Y.-B. Jiang, H. Xu, S. Hersee, and S.M. Han, *Appl. Phys. Lett.* **85**, 1928 (2004).

[32] Q. Li, J.L. Krauss, S. Hersee, and S.M. Han, *J. Phys. Chem. C* **111**, 779 (2007).

Chapter 2

Experimental techniques, setup, and procedures

This chapter introduces the experimental equipment, techniques, and procedures used for the investigations comprising this Thesis. The first three sections, 2.1–2.3, address the techniques used to create and characterize the surfaces: molecular beam epitaxy (MBE), scanning tunneling microscopy (STM), and scanning tunneling spectroscopy (STS). Section 2.4 describes the particular experimental apparatus and procedures.

2.1 *Molecular Beam Epitaxy*

The technique used to deposit Ge on Si during these experiments was a small-scale form of molecular beam epitaxy (MBE) [1]. MBE is a crystal growth technique used to grow high-purity semiconductor structures in an epitaxial, or layer-by-layer, fashion (from the Greek *epi taxis* meaning "form from above"). A general description of the MBE process [2] is as follows and shown in Figure 2-1: the material to be deposited (*source*) is evaporated in ultra-high vacuum (UHV), wherein the evolved atoms or molecules are deposited on a *substrate* material. If the source material is the same as the substrate (e.g., Si on Si), the process is called *homo*epitaxy. Conversely, *hetero*epitaxy is the process of depositing a material chemically different than that of the substrate (e.g., Ge on Si). The primary factors regarding MBE focus on the source and the substrate.

The growth rate of the epitaxial film is largely controlled by the source temperature. The source material is heated to near its melting point to generate a sufficient vapor pressure, which determines the flux of particles emitted: a higher temperature results in a higher particle flux and

thus a faster growth rate. The mean free path of the atoms/molecules evolved from the source is large enough such that, when collimated by an aperture, a 'molecular beam' results. This molecular beam impinges upon the substrate, which is in proximity to the source. Because MBE is a line-of-sight growth technique, the beam can be modulated (i.e., turned 'on' and 'off') with the use of a shutter over the aperture to precisely control the exposure of the substrate to the molecular beam. The shutter also ensures that any transient effects (e.g., source heating up to desired temperature) does not affect the deposition rate, and that one is depositing material only when desired.

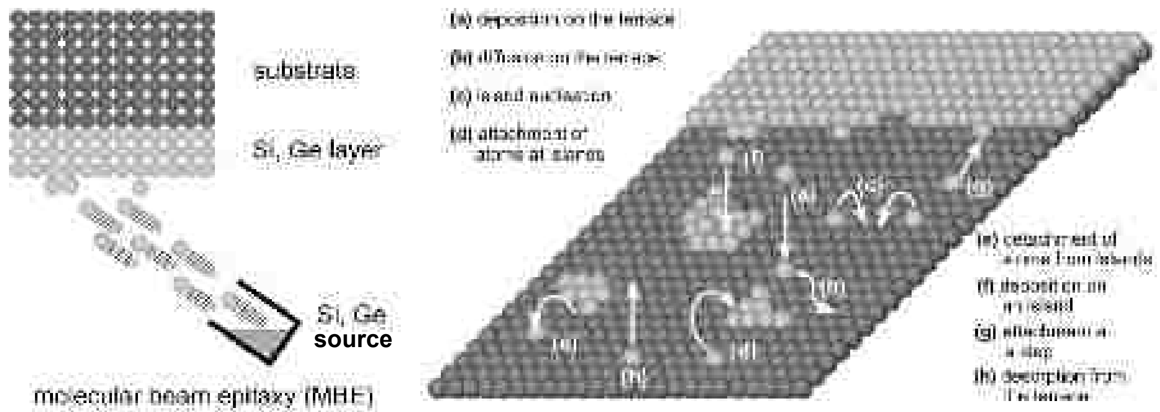

Figure 2-1. Schematic of MBE and surface processes of adspecies. Material is evaporated from the source, and travels as a molecular beam depositing on the substrate as epilayers. Some of the processes adspecies may undergo once adsorbed on the surface. (from [3])

Once the incoming particles of the molecular beam adsorb onto the surface of the substrate, these so-called *adspecies* (a portmanteau of *ad*sorbed and *species*) will become part of the growing film, or epilayer. The substrate is often maintained at some particular elevated temperature during MBE growth to provide sufficient energy for the adspecies, enabling them to undergo a variety of processes, examples of which are shown in Figure 2-1. The kinetics of these processes are also governed by the substrate temperature, and as such, it is an important parameter in MBE [4]. The adspecies should ideally possess enough kinetic energy to thoroughly explore the

potential energy surface of the substrate, ensuring an equilibrium structure is grown. Indeed, if the temperature is too low the adspecies may not have enough thermal energy and simply stick where they adsorb, becoming nucleation sites for island formation. Alternatively, if the substrate is too hot adspecies may have too much energy and desorb from the surface, thus preventing growth.

The interplay between the rates of the various processes occurring during MBE growth (i.e., molecular beam flux and the various surface processes of the adspecies), and other factors can influence the growth mode (e.g., layer-by-layer vs. islanding), and thus the types and qualities of the grown films [5]. Indeed, growth via MBE is often regarded as much an art as it is a science by its practitioners. Regardless, this growth technique is ideal for growing complex, multilayer semiconductor devices (i.e., lasers and LEDs) because it allows for very precise control over the composition of epilayers and the formation of abrupt interfaces. For a thorough treatment of the many aspects regarding MBE the reader is referred to the books in References 6–8.

2.2 *Scanning Tunneling Microscopy*

2.2.1 *General Description*

The scanning tunneling microscope (STM) is an instrument capable of providing atomic resolution images of metal or semiconducting surfaces. Atomic resolution is achievable in part because STM is not an optical imaging technique, so resolution is not diffraction limited. The following is a brief, generic description of the process by which an STM functions: A fine, sharp, metallic probe (usually made of tungsten, platinum-iridium alloy, or gold) is brought extremely close (approximately 5–10 Å) to a metallic or semiconducting surface, in vacuum. When a bias voltage (of the order of a volt) is applied to this junction, electrons can traverse the vacuum gap, giving rise

to a small current (order of nano-ampere). This current is monitored as the probe is scanned across the surface, and used to generate an atomic resolution image of the surface.

As one might expect, such an instrument has enormous potential in many areas of science. So much so, that Gerd Binnig and Heinrich Röhrer were awarded the 1986 Nobel Prize in physics for its invention in 1982 [9]. Since their first published images of the (7×7) unit cell of the reconstructed Si(111) surface in 1983 [10], the capabilities and versatility of the STM have been vastly expanded. In addition to the ability to *passively* characterize surfaces and surface phenomena, STM has been used to alter the surface and influence processes taking place thereon [11–13]. In fact, over the last few decades, STM has served as a harbinger of an entire family of related techniques, collectively referred to as scanning probe microscopy and spectroscopy (SPM/SPS) [14,15], many of which probe a particular property of the surface, such as magnetism. These techniques have enabled scientists to investigate a variety of interfacial properties and surface phenomena at unprecedented scales, benefiting materials science across a broad range of areas [16–18] including catalytic materials, semiconductor surfaces, and biological interfaces, to name a few.

2.2.2 *STM theory*

To better understand how the STM is used to accomplish the above myriad capabilities, we now consider how the STM functions from a theoretical standpoint. As its name implies, the essential principle underlying the functioning of the STM is the phenomenon of quantum mechanical *tunneling*. Tunneling is a process whereby a particle having a total energy lower than a *finite* potential barrier may exist within or beyond that barrier with some finite, albeit small, probability. From a classical standpoint this notion is absurd—surely whether or not an object can penetrate a barrier if its total energy is lower than the barrier's is not questionable. However, the possibility of tunneling derives from the probabilistic nature of particles on the quantum scale. The solution of

the Schrödinger wave equation for electrons within a finite potential barrier can be described by a wavefunction Ψ of the form $\Psi(z) = \Psi(0)e^{-\kappa z}$ [19]. In other words, there is some very small probability of penetration into the barrier [Figure 2-2(a)], which is proportional to the inverse exponential of distance. Thus, if the potential barrier is thin enough, the electron can 'tunnel' through to the other side [Figure 2-2(b)].

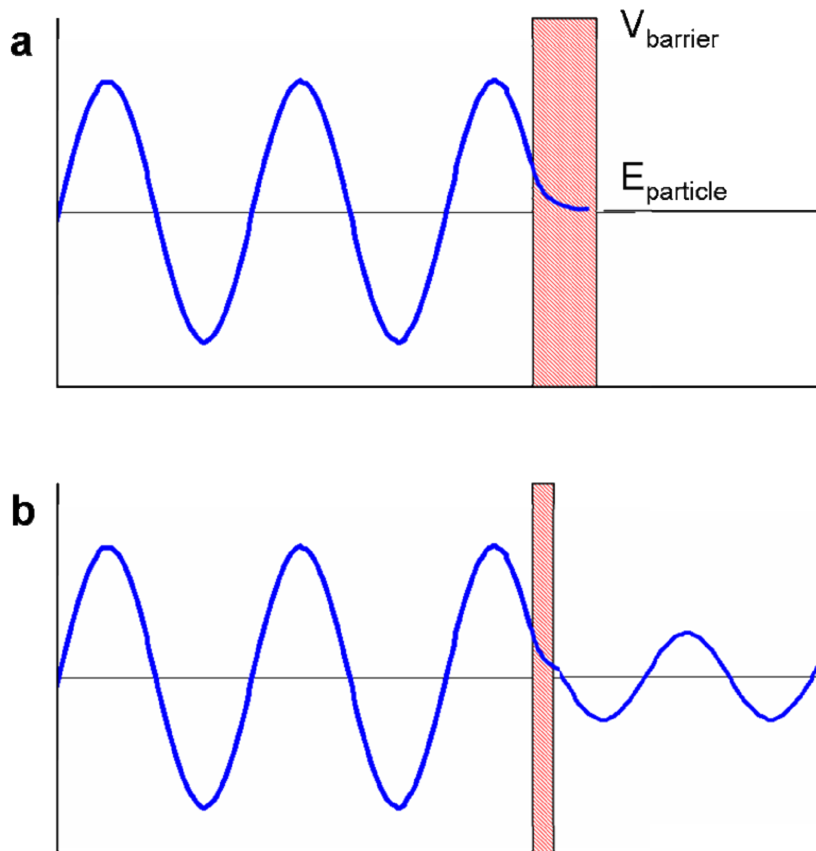

Figure 2-2. Illustration of the concept of tunneling. When the total energy of a particle is less than a finite potential barrier, (a) the probability of the particle existing in the potential barrier decreases exponentially with distance. (b) If the distance is small enough, then it is possible for the particle to emerge on the other side with the same energy, but smaller probability.

Now we can see how the phenomenon of tunneling applies within the framework of STM. For instance, when the probe is brought within proximity to the surface in vacuum, a junction is formed such that the vacuum gap between the probe tip and surface presents a substantial potential barrier. However, this barrier is not infinite, so the electron wavefunctions of the atoms from the

probe tip and surface extend into the gap, and when this gap is small enough, as in the case of STM, the wavefunctions can overlap. The overlapping of the wavefunctions, combined with a junction bias, drives electrons to tunnel across the vacuum barrier. The movement of these tunneling electrons gives rise to a so-called tunneling current, which is extremely small, typically of the order of 100 picoamperes. Nonetheless, it is this small but existent tunneling current that allows the STM to function.

Once a tunneling current is established between the probe tip and surface, we can use it to generate a topograph of the atomic surface structure by the *scanning* aspect of STM, as shown in Figure 2-3. As the probe is scanned across the surface in a raster fashion, any changes in the surface topography will change the tip-surface separation, and thus the tunneling current. The tunneling current is exponentially dependent on the distance between the tip and the surface ($I \alpha e^{-2\kappa z}$), where κ is a characteristic decay length, so that a change in separation of 1 Å results in an order-of-magnitude change in the tunneling current [14,15]. This extreme sensitivity of the tunneling current on separation is what gives STM such superb vertical resolution (~0.1 Å).

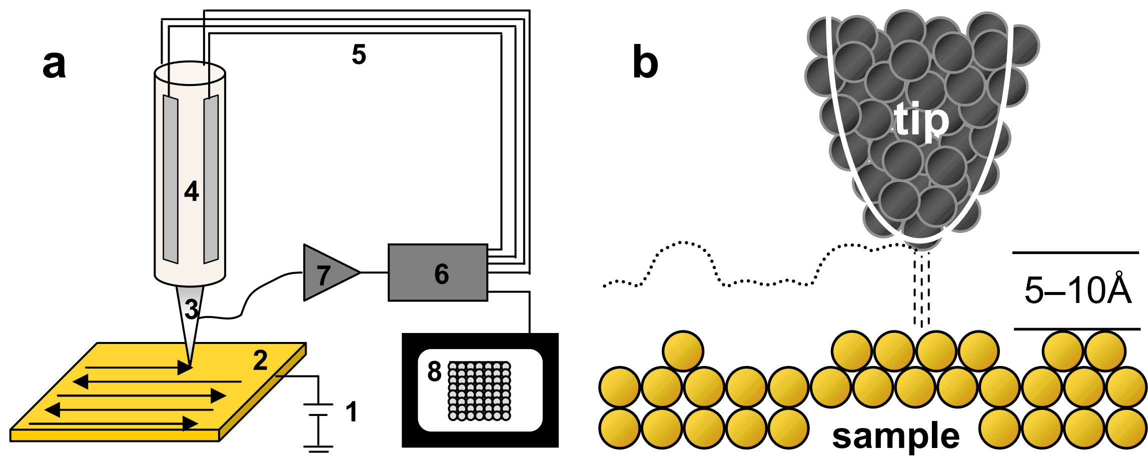

Figure 2-3. Schematics illustrating the STM process. (a) A generalized STM setup: 1. sample bias (tunneling voltage); 2. sample; 3. probe tip; 4. piezoelectric tube with electrodes; 5. control voltages for piezotube; 6. feedback electronics for distance control and scanning; 7. tunneling current preamplifier; 8. display for data processing. (b) Close-up view of tip-sample interface showing the tip tracing out the atomic corrugations of the surface.

As the probe is scanned across the surface, one of two things may happen depending on the imaging mode: (1) In *constant-current* mode, the tunneling current is kept constant, so the instrument must adjust the tip-sample separation accordingly to compensate for changes in tunneling current. (These adjustments are accomplished via a feedback circuit and piezoelectric control elements, usually with sub-Å resolution.) So, if the tunneling current increases, the instrument retracts the tip from the surface and vice versa. In this way, a map of surface topography $z=f(x,y)$ is generated. In which case, the data correspond to contours of constant charge density of the surface [14,15,20]. (2) In *constant-height* mode, the instrument maintains a constant z-position regardless of the change in tunneling current, creating a map of $I=f(x,y)$. For the investigations contained herein, the constant-current imaging mode was used.

2.3 *Tunneling spectroscopy with the STM*

2.3.1 *General description*

As discussed in Section 2.2, the STM principally operates by the electrical conduction of tunneling electrons between the surface and the probe. However, the above description regarding the tunneling process in STM was somewhat simplified. Although the magnitude of the tunneling current is primarily dependent on the tip-sample separation, it is also a function of the electronic structures of the surface and tip, and applied bias voltage. As a result, STM images are inherently a convolution of topographic and electronic information [14,15]. Investigating and interpreting the electronic contributions is the purpose of tunneling spectroscopy.

Due to the presence of covalent bonds in semiconductors, the surface electronic structure has a significant influence on the interpretation of the resulting images. Therefore, understanding the electronic structure of a surface is important because many surface processes (e.g., nucleation,

diffusion, and reactions) are associated with active sites, which may take the form of defects, adsorbates, or other surface features. Moreover, a key advantage of tunneling spectroscopy with STM is the ability to probe surface electronic structure with atomic resolution, so it is possible to associate electronic structure with physical characteristics of the surface. To understand how tunneling spectroscopy is used to investigate the electronic structure of semiconductor surfaces, and the importance of such information, we briefly examine the structure and physics of semiconductors.

2.3.2 *Structure and physics of semiconductors*

The *electronic structure* of semiconductor materials is largely determined by their *physical structure*, i.e. crystal structure [15,20]. For instance, silicon is known to bond in the diamond cubic crystal structure, wherein each bulk Si atom is bonded to four adjacent Si atoms, resulting in a tetragonal geometry [21]. This bonding geometry results from orbital hybridization, as each silicon atom constructs four tetragonally-arranged sp^3 hybridized orbitals from one s and three p orbitals as shown in Figure 2-4. Thus, when sp^3 orbitals from two adjacent Si atoms interact, a covalent sigma σ bond is formed. As a result of this bonding, the sp^3 orbitals split into a lower energy *bonding*, and a higher energy *antibonding* molecular orbital. Now, in a single crystal of Si, the number of atoms bonded together approaches Avogadro's number, and as such represent an ensemble of interacting particles. Moreover, electrons, being fermions, each require a distinct quantum state as consistent with the Pauli Exclusion Principle [22]. To satisfy this quantum-mechanical requirement, the bonding and antibonding energy levels split, respectively, into a valence band and a conduction band, which are comprised of discrete, allowable energy levels. These bands are separated by a so-called band gap, which represents a 'forbidden range' of energies for electrons.

The distribution of electrons in the valence and conduction bands is governed principally by two quantities: the density of states (DOS) and the Fermi-Dirac distribution function, $f_F(E)$. The density of states is a function of energy *and* the physical extent of the crystal, and so represents the number of *available* quantum states at a particular energy per unit volume [21]. The valence and conduction bands are each characterized by a DOS function that is proportional to $E^{1/2}$ [red curves in Figure 2-5(a)], but may have different eccentricities depending on the relative values for the electron and hole effective masses [21].

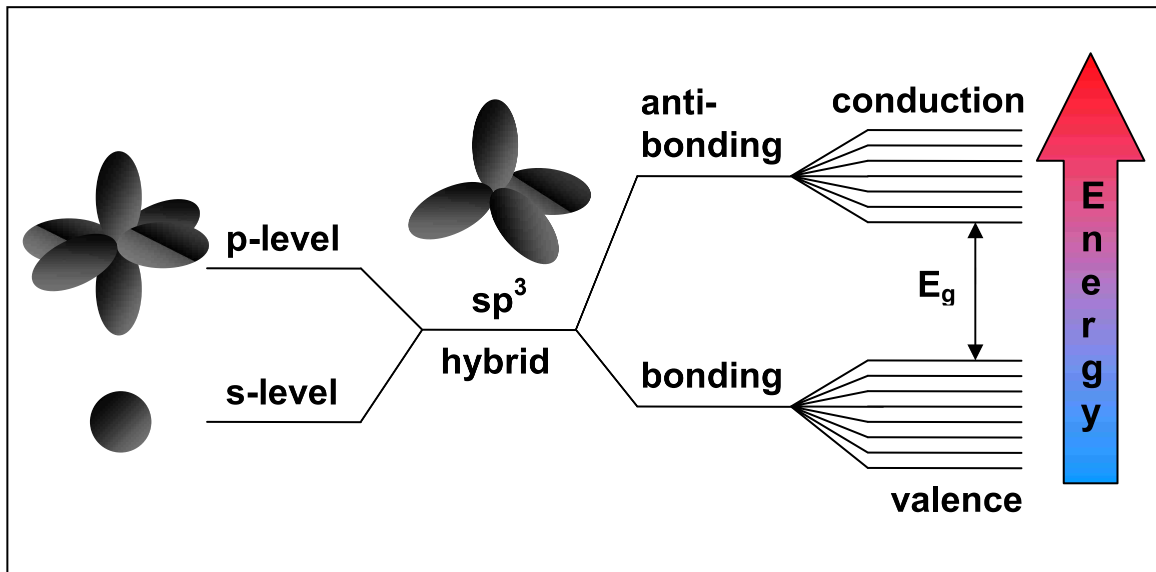

Figure 2-4. Semiconductor band formation energy level diagram. Orbital hybridization allows covalent bonding which gives rise to bonding and antibonding molecular orbitals that each split into the valence and conduction bands in a crystal.

While the DOS describes the *potential* availability of allowed quantum states for electrons, the *probability* of whether or not a particular state is occupied is determined by the Fermi-Dirac distribution function [Figure 2-5(b)]. This probability distribution is temperature dependent, and has an associated Fermi energy E_F, defined as the energy level below which, there is unity probability for occupation by electrons, and above which there is zero probability at T=0 K [21]. At temperatures above 0 K, thermal energy causes some of the electrons to transition to higher

energy levels (in the conduction band) leaving behind an equal measure of vacancies (holes) in the valence band, which changes the shape of the distribution from a Heaviside function [dashed blue line in Figure 2-5(b)], to a sigmoid (solid blue curve). The product of the DOS function and the Fermi-Dirac probability function $g(E)f_F(E)$ gives the density of occupied or filled electronic states (electrons) in the conduction band, whereas the density of unoccupied or empty electronic states (holes) in the valence band is given by $g(E)[1-f_F(E)]$ [light gray curves in Figure 2-5(c)].

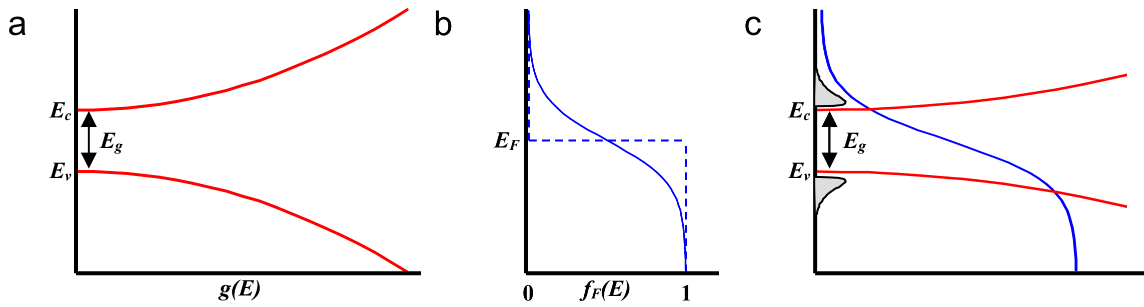

Figure 2-5. Schematics of the DOS and Fermi-Dirac distribution function. (a) The density of allowed electronic energy states *g(E)* for the valence and conduction bands. (b) The Fermi-Dirac probability distribution function shown for T=0K (dashed line) and T>0K (solid line), along with the Fermi energy E_F. (c) The concentrations of electrons in the conduction band and holes in the valence band are shown as light gray regions.

The type of electronic states (filled vs. empty) being imaged during STM can be selected by controlling the polarity of the junction bias, which determines the direction of the tunneling current. For instance, with the sample negatively biased, electrons from filled electronic states in the sample tunnel into the tip; whereas if the sample is positively biased, electrons from the tip tunnel into empty electronic states in the sample. In addition to these conduction/valence band states, there can be so-called *surface states* that exist in the energy range of the bulk band gap. These surface states arise precisely from the existence of a surface (discontinuity of the bulk), which is associated with the formation of dangling bonds. The way in which the surface 'repairs' itself by rebonding is referred to as its reconstruction, and contributes to localized charge density. Finally,

surface states are generally strongly energy dependent and spatially distributed [14,15,20]. The spatial distribution of surface states is called the *local* density of states (LDOS).

2.3.3 *Tunneling spectroscopy techniques*

With the understanding that the geometry, bonding, and crystal structure of a semiconductor gives rise to electronic structure at the surface, we can explore how the scanning tunneling microscope can be used to acquire spectroscopic data. A primary objective of tunneling spectroscopy is to distinguish surface state characteristics such as the LDOS as a function of energy. Various types of spectroscopy can be performed with the STM; however, here we limit our discussion to two—the methods used in the present work.

Voltage dependent spectroscopy

Voltage-dependent imaging is a simple way of obtaining spectroscopic information about a surface using the STM [14,15,23]. This technique is particularly well-suited for semiconductor surfaces because generally their surface states are spatially separated and strongly localized, so voltage-dependent changes in the appearance of the surface can reveal the spatial distribution and energies of surface electronic states. This technique has been used to elucidate the surface structures of GaAs(110) [24], as well as Si(001)–(2×1) [25], for which voltage-dependent data of the latter are presented in Chapter 4. During voltage-dependent imaging, a particular area of the surface is successively scanned at a variety of applied voltages, the *polarity* and *magnitude* of which can be varied. The polarity of the bias voltage determines whether occupied (filled) or unoccupied (empty) states are being imaged, and the magnitude determines the energy. The following implementation of this technique was used in this work: Data at a particular bias are acquired as the STM tip scans from left to right, then the bias is changed (magnitude and/or sign), and the same line is then scanned from right to left. The tip then translates to the next line and repeats this

process in a raster fashion until complete images of the entire surface at the two desired biases are acquired simultaneously.

Scanning tunneling spectroscopy

Scanning tunneling spectroscopy (STS) is a modulation technique used to acquire spectroscopic and topographic information of a surface simultaneously [14,15,26,27]. A high-frequency sinusoidal dither voltage is superposed onto the dc bias voltage that drives the tunneling current. A lock-in amplifier is used to monitor the in-phase ac component of the resultant tunneling current. The resulting data are of the form dI/dV, which is the differential conductance at constant applied bias. This quantity approximates the local density of states (LDOS) [14,15], with maxima corresponding to possible surface states. Thus, during STS a map of conductance is acquired as well as a map of surface topography, so electronic structure in the surface can be correlated to physical features, such as reconstruction. Figure 2-6 illustrates some of the concepts regarding STS.

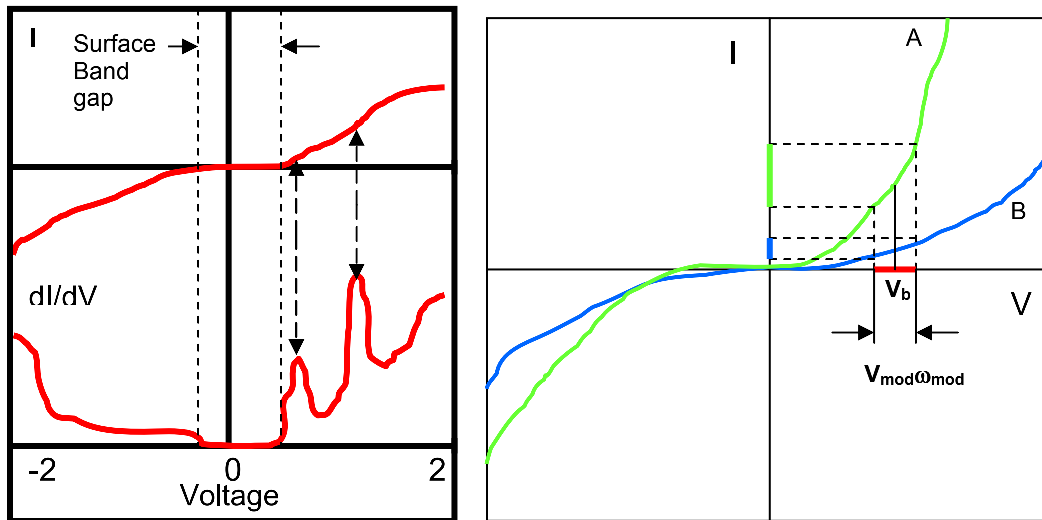

Figure 2-6. Schematics illustrating STS concepts. (Left) Current-voltage characteristics of a surface can reveal surface electronic structure. Inflection points in I-V curve manifest as peaks in dI/dV curve, and indicate possible surface states. Modulation around surface state energies can reveal high-contrast conductance images. (Right) I-V curves for two different materials A and B. At the particular modulation voltage, material A will have a larger differential conductance than material B, and will appear brighter in a conductance image. This concept can be exploited to achieve chemical contrast between different materials in a surface.

2.4 *Experimental setup and generalized procedure*

Experimental setup

All of the necessary equipment used to conduct the experiments is housed in an ultrahigh vacuum (UHV) chamber with a background pressure of $\leq 5\times10^{-11}$ Torr. This base pressure is achieved by multistage pumping (e.g., roughing, turbomechanical, ion, and titanium sublimation) in conjunction with baking the entire system with heaters. The chamber was designed such that most of the critical components (i.e., sample storage stage, sample preparation stage, STM imaging stage, and electrical feedthroughs) are mounted on a single 'utility' flange. This arrangement allows for easy access for maintenance when the flange is removed. The UHV chamber has provisions to transfer new samples into the chamber without breaking vacuum via a load-lock chamber. Inside the UHV chamber, samples are transferred between the various stages with the use of an *xyz* translator equipped with an alligator clamp to hold the sample.

The sample preparation stage is where samples are cleaned and epitaxial growth performed prior to STM imaging. Samples are secured to molybdenum contacts with molybdenum spring clips to ensure good electrical contact, and resistively heated to a desired temperature. The source for epitaxial growth is located about 1 inch from the substrate, and comprises a resistively-heated alumina-coated tungsten wire basket that contains the epitaxial material, and is fitted with a shutter to control exposure of the substrate to the molecular beam.

The STM imaging stage contains a variable-temperature scanning tunneling microscope. Three-dimensional movement of the probe is achieved with a piezoelectric tube scanner. The probe tip is fabricated from tungsten wire that is electrochemically etched. The STM is housed on a copper block that is suspended by four springs and flanked by permanent magnets to dampen

vibrations and movements via induced eddy currents. The entire UHV chamber is mounted on a pneumatically-stabilized table.

Generalized experimental procedure

Silicon (001) samples were pre-cleaned by swabbing both sides with isopropyl alcohol, followed by acetone to remove any organic residues. These pre-cleaned samples are then loaded into the vacuum chamber via the load-lock chamber, or whenever the utility flange was removed during maintenance.

Inside the UHV chamber, a new pre-cleaned sample is taken from the sample storage tray and inserted into the sample preparation stage. The sample is then flash annealed by passing current through the Si sample and heating it by resistive heating. The sample is raised to a temperature of about 1250 °C, as determined using an infrared pyrometer. This process desorbs the native oxide (SiO_2) layer, exposing a clean Si surface. After about 1 minute, the current is instantly shut off, allowing the sample to radiatively quench to room temperature. The result of this sample preparation procedure is a clean Si(001) surface exhibiting 2×1 reconstruction.

This clean Si(001)–(2×1) surface serves as the substrate for further processing and eventual investigation. Germanium is deposited on the Si surface via molecular beam epitaxy to either create an alloyed $Si_{1-x}Ge_x$ ($0 < x < 1$) surface of a particular composition, or to deposit Ge adspecies, depending on the experiment. A SiGe alloyed wetting layer is formed by depositing approximately 1.5 monolayers (ML) of Ge onto the substrate, which is held between 500–600 °C. This preparation results in a SiGe alloy wetting layer exhibiting a periodic $2\times n$ reconstruction ($n\sim10$) with highly ordered dimer vacancy lines. Additional sub-ML Ge deposition on this $2\times n$ SiGe surface is performed to seed the surface with adspecies. Once the desired surface is prepared, it is transferred to the STM imaging stage for microscopy characterization.

2.5 *References*

[1] A.Y. Cho and J.R. Arthur, *Prog. Solid State Ch.* **10**, 157 (1975).

[2] G. Biasiol and L. Sorba, *Crystal growth of materials for energy production and energy-saving applications*, (Eds. R. Fornari, L. Sorba, Pisa, 2001).

[3] B. Voigtländer, *Surf. Sci. Rep.* **43**, 127 (2001).

[4] D. Papajová and H. Sitter, *Semicond. Sci. Technol.* **13**, 1247 (1998).

[5] D.K. Goswami, B. Satpati, P.V. Satyam, and B.N. Dev, *Curr. Sci. India* **84**, 903 (2003).

[6] M.A. Herman and H. Sitter, *Molecular Beam Epitaxy: Fundamentals and Current Status*, (Ed. A. Zehe, Springer-Verlag, Berlin-Heidelberg-New York-London-Paris-Tokyo 1989).

[7] J.Y. Tsao, *Materials Fundamentals of Molecular Beam Epitaxy*, (Academic Press 1992).

[8] *Molecular Beam Epitaxy: Applications to Key Materials*, (Ed. R.F.C. Farrow, Noyes, 1995).

[9] G. Binnig and H. Rohrer, Scanning Tunneling Microscope, (United States Patent 4,343,993) 1982.

[10] G. Binnig, H. Rohrer, Ch. Gerber, and E. Weibel, *Phys. Rev. Lett.* **50**, 120 (1983).

[11] G. Meyer, J. Repp, S. Zöphel, K.-F. Braun, S.W. Hla, S. Fölsch, L. Bartels F. Moresco, and K.H. Rieder, *Single Mol.* **1**, 79 (2000).

[12] S.-W. Hla and K.-H. Rieder, *Annu. Rev. Phys. Chem.* **54**, 307 (2003).

[13] S.-W. Hla, *J. Vac. Sci. Technol. B* **23**, 1351 (2005).

[14] R. Wiesendanger, *Scanning Probe Microscopy and Spectroscopy: Methods and Applications*, (Cambridge University Press, 1994).

[15] *Scanning Probe Microscopy and Spectroscopy: Theory, Techniques, and Applications*, (Ed. D. Bonnell, Wiley-VCH 2 edition, 2000).

[16] J.E. Griffith and G.P. Kochanski, *Annu. Rev. Mater. Sci.* **20**, 219 (1990).

[17] H. Neddermeyer, *Rep. Prog. Phys.* **59**, 701 (1996).

[18] E. Meyer, S.P. Jarvis, and N.D. Spencer, Scanning Probe Microscopy in Materials Science, *MRS Bulletin* p.443 July 2004.

[19] R. Liboff, *Introductory Quantum Mechanics* (4th edition), (Addison Wesley, 2002).

[20] A. Zangwill, *Physics at Surfaces*, (Cambridge University Press, 1988).

[21] D.A. Neamen, *Semiconductor Physics and Devices* (3rd edition), (McGraw-Hill, 2003).

[22] D. Halliday, R. Resnick, and J. Walker, *Fundamentals of Physics Extended* (5th edition), (John Wiley & Sons, Inc., 1997).

[23] J.A. Stroscio, R.M. Feenstra, D.M. Newns, and A.P. Fein, *J. Vac. Sci. Technol. A* **6**, 499 (1988).

[24] R.M. Feenstra, J.A. Stroscio, J. Tersoff, and A.P. Fein, *Phys. Rev. Lett.* **58**, 1192 (1987).

[25] R.J. Hamers, R.M. Tromp, and J.E. Demuth, *Surf. Sci.* **181**, 346 (1987).

[26] R.S. Becker, J.A. Golovchenko, D.R. Hamann, and B.S. Swartzentruber, *Phys. Rev. Lett.* **55**, 2032 (1985).

[27] A. Baratoff, G. Binnig, H. Fuchs, F. Salvan, and E. Stoll, *Surf. Sci.* **168**, 734 (1986).

Chapter 3

Polarity-switching scanning tunneling microscopy of addimer chain structures

In this chapter we discuss the observations, characteristics, and implications concerning a previously unknown adspecies on the Ge-Si(001)-(2×*n*) surface, namely *addimer chain structures* (ADCSs). Information such as the formation, composition, morphological aspects, and dynamics of ADCSs provides a crucial link toward developing a complete and coherent understanding of the various atomic processes occurring during the heteroepitaxy of Ge on Si(001). As such, it is worthwhile to first discuss, in some detail, some of the fundamental atomic processes which occur during epitaxy (first introduced in Chapter 2). This introduction shall serve to establish a suitable context for the discussion of ADCSs.

3.1 *Heteroepitaxy of Ge on Si(001)-(2×1)*

A prototypical SiGe heteroepitaxial growth procedure via molecular beam epitaxy (MBE) was outlined in Chapter 2. One of the principal growth parameters is the temperature of the substrate. The substrate temperature determines, to a large extent, the kinetics, thermodynamics, and growth mode of the epitaxial process. For instance, an elevated substrate temperature allows for a substantial amount of *intermixing* and increased *diffusion* to occur at the surface.

Intermixing is a process whereby neighboring atoms in adjacent atomic layers exchange lattice sites. This process can be especially important in lattice-mismatched growth (e.g. SiGe) because of the implications regarding interface abruptness and stress. While partially entropy-

driven [1], intermixing is one means of reducing the free energy of the growing film by facilitating stress relief [2–4]. Stress may be further reduced by the introduction of strain effects [5], manifesting either as defects or changes in the surface morphology.

Diffusion is the thermally-activated movement of adatoms (and other adspecies), and thus corresponds to their kinetic energy. The kinetic energy (and thus diffusion) of adspecies largely determines to what extent the physical topography and corresponding potential energy map of the surface is explored. In this way, diffusion is intimately related to the types of processes that are energetically available and their rates [6]. Moreover, the kinetics can determine the morphology of the growing surface [7]. (There are many additional aspects of epitaxy that influence the growth mode such as the native surface topography and orientation, surface energies, chemical potentials, and lattice constants [8–10].) For example, if the kinetic energy of adspecies is too low the addimers may tend to cluster, and growth can occur by islanding (i.e., Volmer-Weber growth [11]). However, if their kinetic energy is large enough, the adspecies will diffuse about the surface, resulting in either layer-by-layer (i.e., Frank-van der Merwe growth [12]) or step-flow growth [13,14]. These latter growth modes are preferred, due to fewer defects and higher quality crystal structure (i.e., closer to equilibrium).

The evolution of the SiGe heterosystem during epitaxy [8,15,16] is a model example of the Stranski-Krastanov growth mode [17]—in which a pseudomorphic, two-dimensional wetting layer is initially formed, followed by the nucleation and growth of three-dimensional islands. This growth mode is an intermediary growth mode, as it exhibits characteristics of both Frank-van der Merwe and Volmer-Weber growth. Figure 3-1 is a collection of STM images characterizing the morphological surface phase transitions observed during Stranski-Krastanov growth of Ge on Si(001). Upon Ge exposure, a clean Si(001)–(2×1) surface [Figure 3-1(a)] is transformed into an

alloyed SiGe wetting layer, exhibiting a 2×n reconstruction [Figure 3-1(b)] [3,4,18,19]. For this particular reconstruction, every n^{th} dimer is missing from the surface, forming long-range ordered

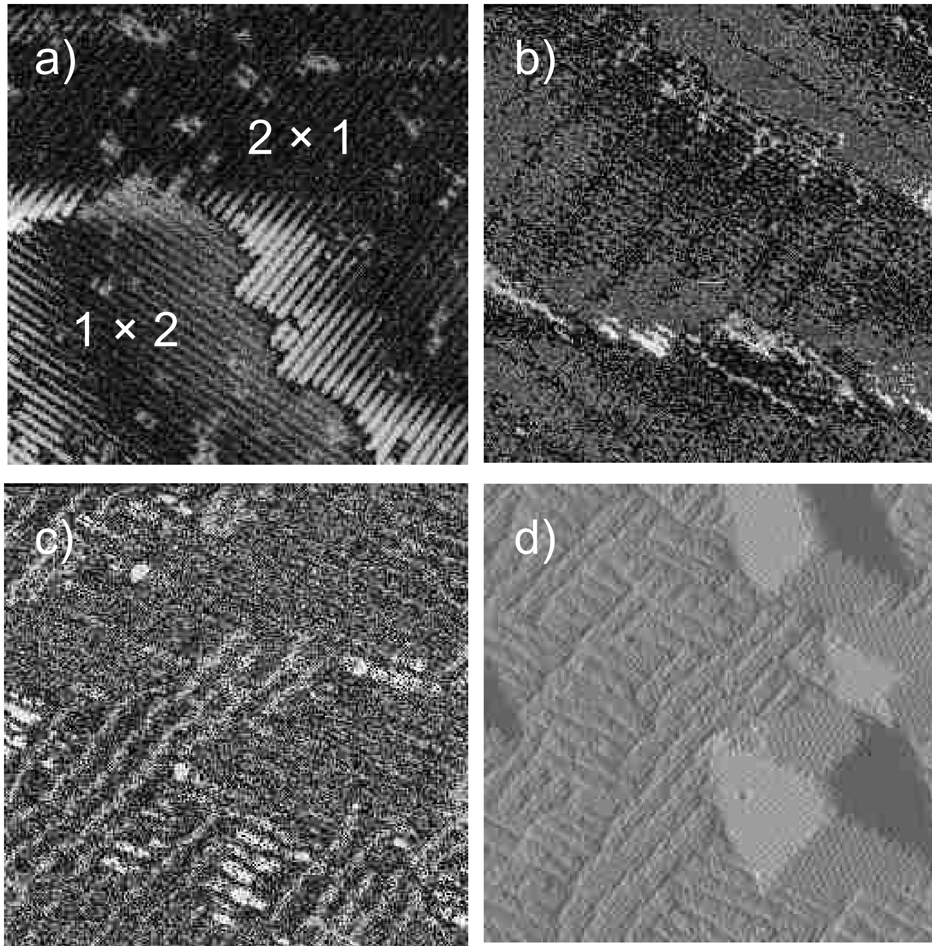

Figure 3-1. **STM images showing the morphological evolution with increasing Ge exposure on Si(001).** (a) 250 Å×250 Å image showing a clean Si(001) surface exhibiting 2×1 reconstructed dimer rows. Missing surface dimer defects are also visible as black spots. (b) 250 Å ×250 Å image of a SiGe alloy exhibiting 2×n reconstruction. The surface dimers are statically buckled giving rise to a honeycomb-like appearance. Dimer vacancy lines periodically punctuate the surface to relieve misfit stress. (c) 500 Å×500 Å image of SiGe alloy wetting layer exhibiting m×n reconstruction. (d) 500 Å×500 Å image showing the presence of quantum 'hut' structures on a m×n wetting layer. (All images are filled-state images obtained at a sample bias of ~ –1.7 V. Note (d) is a derivative image.)

dimer vacancy lines (DVLs) that extend perpendicular to the substrate dimer rows. These DVLs partially relieve misfit stress by accommodating outward relaxation of the compressed substrate dimers [8,18,20]. Additionally, this 2×n surface exhibits a large degree of buckling of the surface

dimers in both $c(4\times2)$ and $p(2\times2)$ phases resulting in a 'honeycomb-like' appearance of the surface. With continuing Ge deposition, a denser $m\times n$ reconstruction appears [Figure 3-1(c)], in which large "belts" of $2\times n$ regions are present [21–23]. The combined $2\times n$ and $m\times n$ surfaces comprise a pseudomorphic wetting layer that persists for ~3 MLs [24]. As Ge is further deposited, the stress in the forming epilayers continues to increase. However, with all 2-D modes of stress relief exhausted, the growth becomes three-dimensional, resulting in the formation of pyramidal 'hut' clusters exhibiting distinct {105} facets [16] [Figure 3-1(d)]. Further deposition results in the transformation of hut clusters into multifaceted islands called 'domes' and 'superdomes' (not shown) [25–27].

As mentioned earlier, diffusion enables adatoms to achieve more stable configurations by locally minimizing their free energy. One of the most common such configurations is that of an *addimer*. An addimer is comprised of two covalently bonded adatoms. On Si(001)– and Ge(001)–(2×1) surfaces, addimers are theoretically predicted [28–32] and experimentally observed [29,30,33–35] to assume any of four possible binding orientations shown in Figure 3-2. These four orientations are distinguished according to their position relative to the dimers composing the surface. For example, addimers may either reside *on* a substrate dimer row (types *A* and *B*) or *in* a trough between two neighboring dimer rows (types *C* and *D*). Additionally, the addimer bond direction can be *parallel* to the substrate dimer bonds (types *A* and *C*) or *perpendicular* to them (types *B* and *D*). While all these addimer adsorption configurations are local energy minima, they are not equally favorable. For instance, theoretical calculations [28,31,32] for single Si addimers on Si(001) predict *on-top* dimers (*A* and *B*) to be more stable than *in-trough* dimers (*C* and *D*).

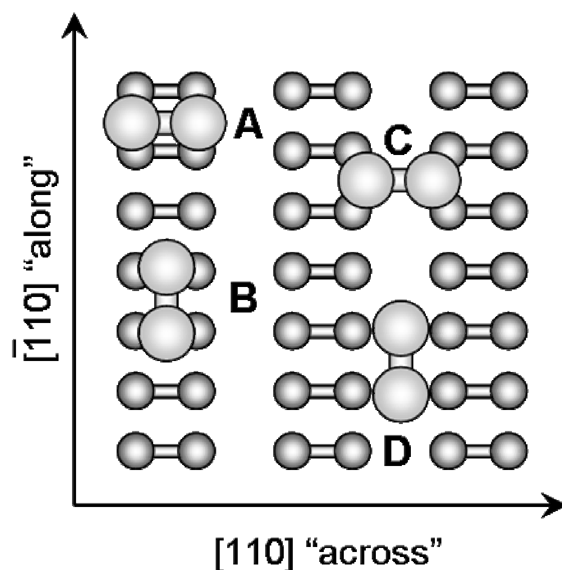

Figure 3-2. Various addimer adsorption sites, orientations, and nomenclature for a (2×1) surface. The use of the terms *along* and *across* with respect to substrate dimer rows correspond to [1¯10] and [110] directions, respectively.

These predictions have been supported by experimental observations using STM [29,35,36], in which *on-top* addimers are more commonly observed than *in-trough* dimers. The relative energies of *on-top* dimers (*A* and *B*) are nearly degenerate, although the epitaxial configuration (*B*) is slightly favored. A low activation barrier allows the addimers to rotate freely between the two configurations at room temperature [30]. As for the less stable *in-trough* dimers; *C*-dimers are a metastable configuration whose formation is dominated by kinetics [33], while isolated *D*-dimers have never been observed [33].

The relative stabilities of the addimers can change when adstructures, composed of multiple addimers, are formed [32]. For instance, two commonly observed adstructures for the Si(001)–(2×1) surface are the *dilute-dimer row* (DDR) and *compact epitaxial island* (CEI) [31–35,37,38]. The dilute dimer row is a linear arrangement of *C* dimers occupying neighboring *in-trough* sites, alternating with vacant *on-top* sites, extending across the substrate dimer rows in ⟨110⟩

directions (i.e., -*C*-*C*-*C*-…). The appearance of DDRs in filled-state STM topographs resembles a 'string of pearls,' as shown in Figure 3-3(a).

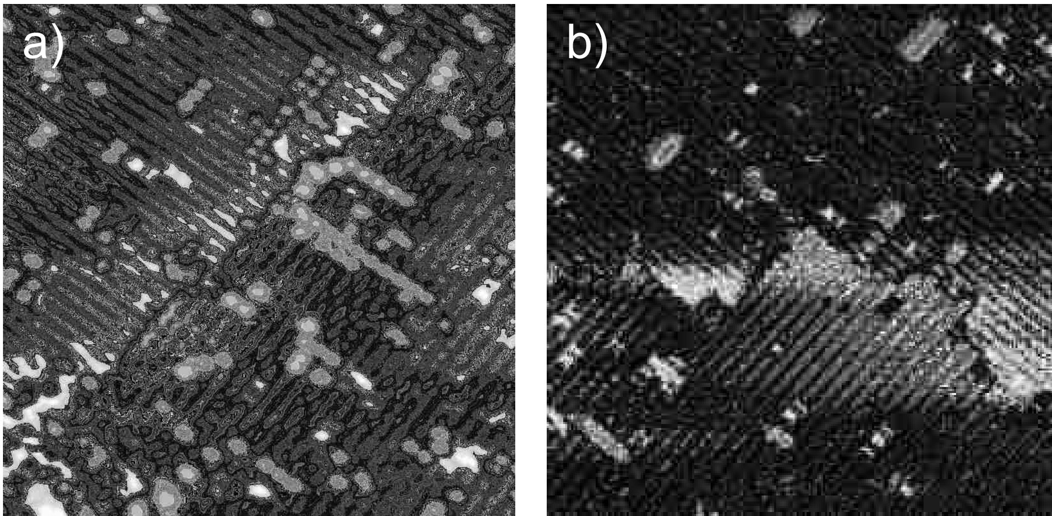

Figure 3-3. Sub-ML Ge coverage on Si(001). (a) Ge deposited on a substrate at room temperature forms dilute dimer rows (DDRs) that appear as 'strings of pearls.' (b) Ge deposited on a 'hot' substrate (~250 °C), allowing for substantial Ge adatom diffusion resulting in the formation of compact epitaxial islands (CEIs).

Compact epitaxial islands are similar to DDRs in that they also extend across the substrate dimer rows in ⟨110⟩ directions; however, they do not contain any vacant sites, and thus are denser than DDRs. They consist of alternating *on-top* and *in-trough* addimers arranged in an epitaxial fashion (i.e., BDBD). Furthermore, annealing treatments demonstrate that CEIs are thermodynamically favored over DDRs [38].

3.2 *Heteroepitaxy of Ge on Ge-Si(001)-(2×n)*

Many of the same processes and concepts introduced in the last section on silicon are relevant to SiGe surfaces: intermixing, diffusion, addimers, and adstructures. However, there are some notable differences. Some of these differences are apparent by comparing Figures 3-3 and 3-4. Immediately noticeable is the difference in surface reconstruction. The Si(001) surface (Figure 3-3)

is 2×1 reconstructed, with bean-shaped dimers that appear symmetric due to dynamic buckling [39–41]. Alternatively, the 2×*n* reconstructed SiGe alloy surface (Figure 3-4) displays a 'honeycomb-like' appearance, in which the substrate dimers are statically buckled out of the surface plane in either *c*(4×2) or *p*(2×2) phases. Moreover, while both surfaces are partially covered with sub-ML Ge, there are different types of addimers and adstructures present on each surface. As shown in Figure 3-4, CEIs and on-top addimers (white circle) are easily seen in both filled- and empty-state STM images. However, a new type of adstructure for the SiGe 2×*n* surface, which we term *addimer chain structures* (ADCSs), are only seen easily in empty-state images (white rectangle). In filled-state images ADCSs are virtually invisible, appearing only as faint 'ghost-like' features with an associated disturbance to the buckling of the underlying substrate dimers [33,42,43]. In light of the dramatic differences between filled- and empty-state images of ADCSs, the polarity-switching STM technique is essential to their study.

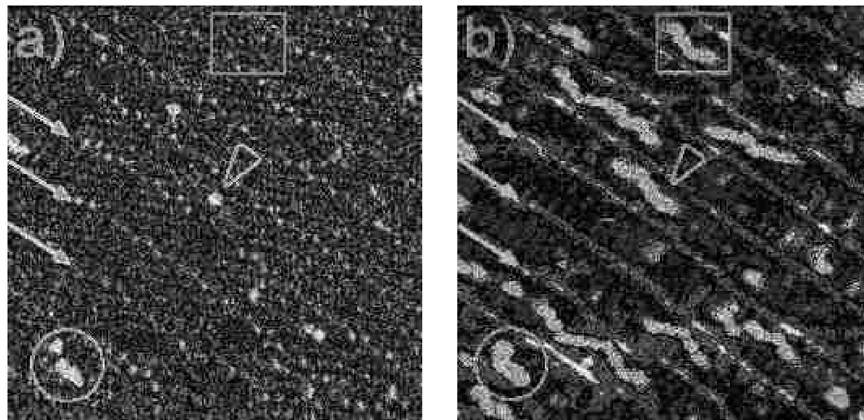

Figure 3-4. STM images (200 Å × 200 Å) of the 2×*n* reconstructed SiGe wetting layer after sub-ML Ge deposition. The dimer vacancy lines are seen to run across the images at ~45°. Three vacancy lines are identified by white arrows. (a) Filled-state image (–1.7 V) showing a highly buckled, 'honeycomb-like,' *c*(4×2) surface and very little apparent surface adspecies, which appear as white features. Note that the faint 'ghost-like' areas of disturbed substrate dimers (one such area is outlined by a white rectangle) correspond to the presence of ADCSs, which are easily seen in (b), a corresponding empty-state image (+1.7 V). Epitaxial islands are clearly visible in the lower left corner in both biases, outlined by a white circle. The triangle identifies a C-dimer in a linear structure.

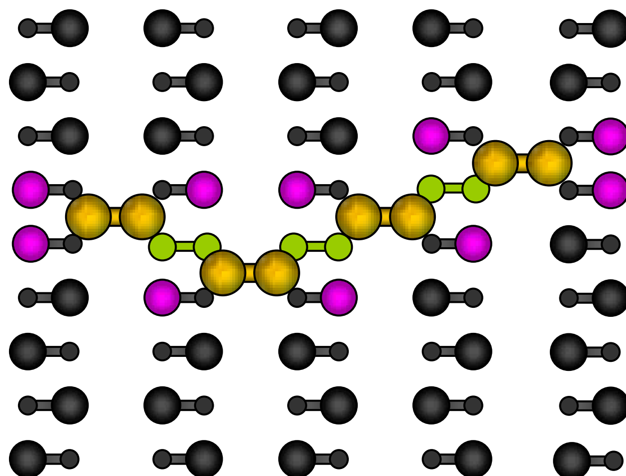

Figure 3-5. Schematic illustrating the relative positions of the constituent C-dimers (gold) of an ADCS in relation to substrate dimers. The surface dimers are statically buckled out of phase in a *c*(4×2) reconstruction. The phase of buckling on a particular dimer row changes 180° across an ADCS. The purple atoms indicate dangling bonds neighboring the ADCS.

ADCSs consist of chains of C-dimers residing in neighboring in-trough positions, and are thus dilute structures, similar to DDRs. However, unlike DDRs, which extend along ⟨110⟩ directions, ADCSs extend across the substrate dimer rows in all equivalent ⟨130⟩ directions, at ~63° with respect to the substrate dimer bonds as shown in Figure 3-5. This orientation results in C-dimers being offset one lattice site, above or below, with respect to its neighboring C-dimer, giving rise to a zigzag morphology. We further observe that ADCSs range in length from two to about twelve units of C-dimers; however, the most commonly observed lengths are 2–5 units. (We also observe isolated C-dimers, but by definition they do not constitute a chain structure.) Finally, it should be noted that similar chain structures have been observed on all of the permutations for the silicon-germanium system: Si on Si(001) [33,44], Ge on Si(001) [45], Si on Ge(001) [46], and Ge on Ge(001) [42,43].

3.3 *Formation of ADCSs*

We observe ADCSs to predominate on $2\times n$ reconstructed SiGe alloy surfaces after Ge deposition at *room temperature*. This observation implies that *only* adatoms are responsible for the formation of ADCSs, because the diffusion of addimers at room temperature is not energetically favorable [36–38,46–50]. However, at elevated temperatures it is possible that addimer diffusion is activated, allowing them to become involved in the formation mechanism. Indeed, Galea *et al.* [43] investigated similar chain structures for the Ge on Ge(001) system, where the diffusion of addimers at room temperature is appreciable. Thus, they suggested that the formation mechanism may involve either addimer or adatom incorporation. However, even at temperatures up to 150 °C, we observe ADCSs to exhibit only *localized* movement, which we discuss in the next section. Single monomers, on the other hand, are *extremely* mobile at room temperature [28,51–57], such that their diffusion cannot even be resolved by STM. (One approach to overcome this setback involves reducing the experimental temperature to less than 200 K, to slow down the kinetics of adatom diffusion [58].) However, even at room temperature, monomers can be observed bound in proximity to type S_B step edges and islands [59]. These sites had previously been shown to be local energy minima, with a correspondingly substantial binding activation barrier via theoretical investigations [60–64]. Monomers have also been predicted [31,32,44] and observed to bind near C-dimers [33–35,46] (and D-dimers [65]) to form three-atom clusters that are suspected to serve as growth nuclei. Similarly, we have observed adatoms attached to the ends of ADCSs, as shown in Figure 3-6.

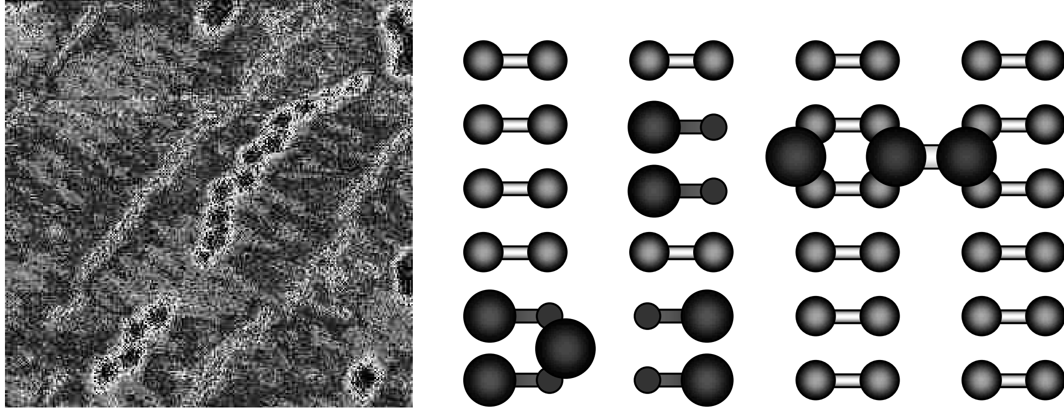

Figure 3-6. **Monomer binding sites.** Ten-unit ADCS with a single monomer (adatom) bonded at the M-site in a ⟨110⟩ direction with an end addimer. The adatom appears roughly half the size of a normal addimer. The schematic represents adatom-induced buckling and M-site adsorption.

This aspect of *monomer trapping* at islands underlies the herein proposed mechanism of ADCS formation and growth, which we term the Adatom-Trapping-Addition (ATA) mechanism. As its name suggests, the primary steps in the formation mechanism include (see Figure 3-7): (1) a thermal adatom diffusing on the surface encountering another adatom, thereby nucleating an addimer, which is a more stable species. This stable—and virtually immobile—addimer now serves as a nucleus for further growth leading toward an ADCS. (2) It is now possible for a diffusing adatom passing-by this trough-dwelling *C*-dimer to become ensnared, binding at the so-called M-site shown schematically in Figure 3-6. The M-site corresponds to the position in a trough between two surface dimers [44,52,56–58]. (3) This trapped adatom is now rendered temporarily immobile at this local energy minimum (M-site) inline along a ⟨110⟩ direction with its 'captor' addimer. (4) Subsequently, it is now possible for another adatom diffusing along the same dimer row to encounter the trapped adatom, possibly resulting in the formation of a new addimer. When the new addimer is formed, it must rearrange so as to align in a ⟨130⟩ direction thereby extending the ADCS. This mechanism is likely complicated in that it involves adatom-addimer interactions and simultaneous rearrangement of the substrate dimers (i.e., multi-body interactions)

[35,42,43]. Indeed, similar mechanisms are speculated to occur for dilute dimer rows [31–33], and have been likened to the so-called surface polymerization seen in Al on Si(001) [66].

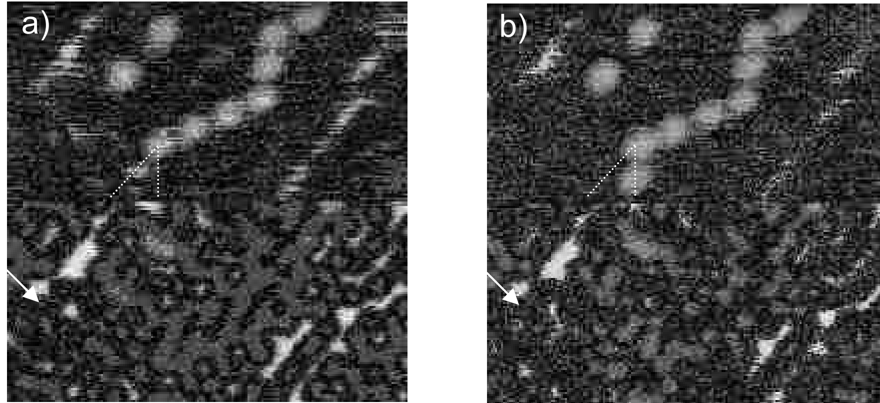

Figure 3-7. Adatom-Trapping-Addition mechanism. STM images demonstrating the proposed ATA mechanism possibly responsible for ADCS growth. (a) (top frame, empty state) A trapped adatom is 'in line' along a ⟨110⟩ direction with an end addimer of an ADCS. Presumably, upon diffusion of another adatom, (b) a new *C*-dimer is formed and rearranges to a ⟨130⟩ orientation. Filled state images (bottom frames) in (a) and (b) demonstrate the concomitant rearrangement of the substrate dimer row involved with the ADCS extension (indicated by the white arrows).

Because ADCSs are metastable structures (as evidenced by their transition to CEIs), the ATA formation mechanism is likely determined by kinetics [33,35,44–46]. As a consequence, the two principal steps of the ATA mechanism will have an associated characteristic time or rate: the trapped adatom residence time and the adatom arrival rate. The growth of ADCSs is then determined by a competition between the rates of these two processes. Moreover, both of these processes should be temperature-dependent, while the adatom arrival rate will also be a function of the adatom concentration on the surface as set by the Ge flux.

3.4 *Mobility of ADCSs*

ADCSs often contain straight and kinked segments, which gives rise to a zigzag morphology. We distinguish and categorize the multiple C-dimers that constitute an ADCS according to their relative positions in the chain structure (see Figure 3-8). For example, every ADCS has two *end* units (1 and 5 in Figure 3-8), each with only one nearest neighbor. Of the interior addimers, a unit is designated a *kink* (gray dots in Figure 3-8) if both its nearest neighbors are in line with each other along a ⟨110⟩ direction, or a *straight* if it maintains a ⟨130⟩ direction [checkered dot, Figure 3-8(a)].

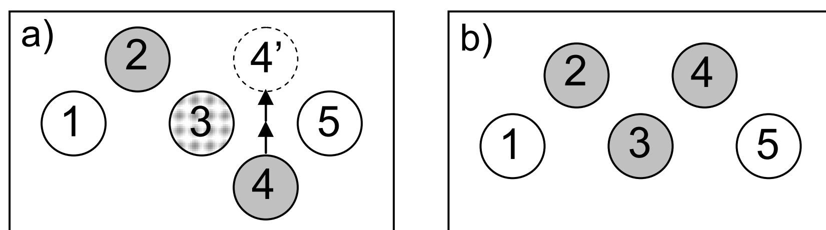

Figure 3-8. **Orientation and nomenclature for ADCS constituent addimers.** Schematic defining 'ends' (white), 'kinks' (gray), and 'straights' (checkered) depending on the relative positions of addimers in an ADCS. (a) After Kink 4 diffuses two lattice sites, indicated by the arrows, (b) it changes the designation of its neighbor, 3, from a straight to a kink.

Over the temperature range studied (90–150°C), ADCSs are observed to exhibit localized movement of their constituent C-dimers such that the ADCSs generally remain intact. Consequently, we do not observe long-range diffusion of the C-dimers, even at 150 °C. Such dynamics require potentially mobile units (ends or kinks) to undergo double-jump diffusion in a manner so as to preserve ⟨130⟩ orientations and continuity of the chain. In fact, STM movies show ADCSs to move with almost 'snake-like' undulating motions. Moreover, ADCS dynamics are characterized by the constituent C-dimers generally moving in directions along the substrate dimer rows. We have occasionally observed the movement of end C-dimers to diffuse away from a chain structure, across dimer rows; however, such behavior is not commonplace, presumably because the activation energy for diffusion in this direction is larger. After all, anisotropic diffusion is well

established with Si and Ge monomers and dimers on Si(001) and Ge(001) surfaces [31,36,42,43,46,49,52–56,67–70]. Finally, we observe that end units are generally more active than interior units, which is in accord with observations of Ge chain structures on Ge(001) [43].

Figure 3-8 illustrates an example of one possible way for a five-unit ADCS to rearrange. When a mobile unit (Kink 4) makes a double jump to its mirror lattice site 4', the designation of one of its neighbors,3, changes from a straight to a kink. However, this rearrangement does not affect the relationship of the dimer that jumped (4) with respect to its nearest neighbors (3 and 5): it is still a kink, due to symmetry. This move does, however, change the relative orientation with respect to its next-nearest neighbor (Kink 2). If a straight were to undergo such double-jump diffusion, the chain would break apart into two ADCSs. This is not to imply that such a maneuver is impossible, only that for the ADCSs studied over this temperature range, we generally do not observe such behavior, implying that the energetic barrier for this process is too large. Moreover, this observation is also consistent with that of Galea *et al*. [43] who report, "the observed displacements are always such that locally the ⟨130⟩ alignment is conserved" for similar chain structures of Ge on Ge(001). In this regard, it appears as though the C-dimers in an ADCS stabilize each other through 'attractive' interactions, perhaps via substrate-strain-mediated coupling [34,58,71–73]. In addition to this typical behavior, we observe a rare exception: When a C-dimer cannot diffuse to its mirror lattice site because of surface defects. In this case, the C-dimer can diffuse only one lattice site, resulting in a linear structure along a ⟨110⟩ direction, analogous to a dilute dimer row. And, also like a dilute dimer row, the C-dimer in this linear segment now appears in both empty- and filled-state images (pointed by a triangle in Figure 3-4). However, this is an unstable configuration for the chain structure, and it quickly assumes its original ⟨130⟩ position.

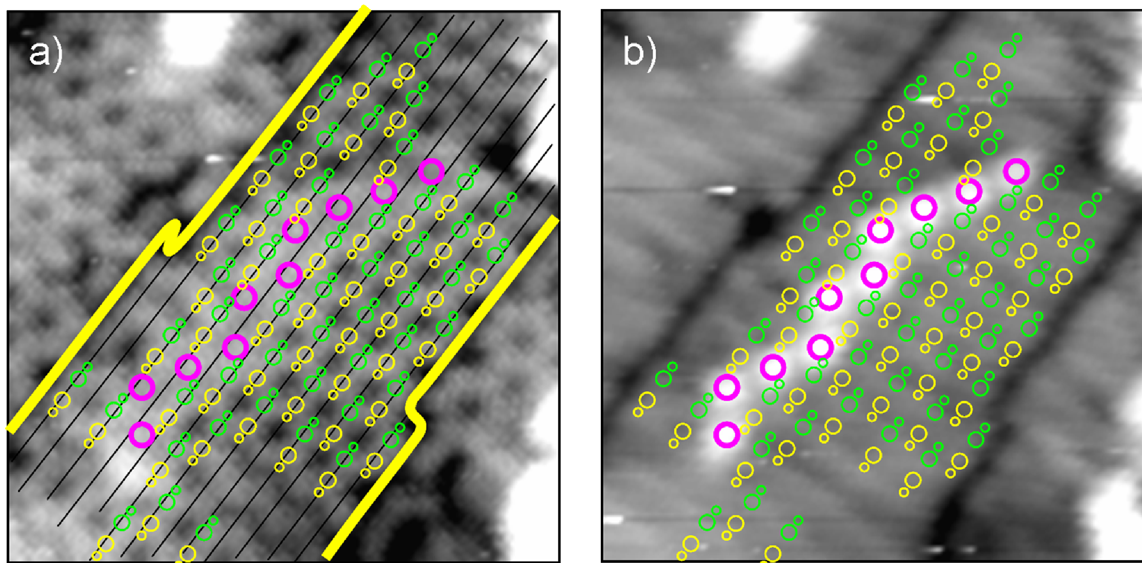

Figure 3-9. **ADCS-induced phase shift in buckling registry of surface dimers.** The pink circles overlay the C-dimers of the ADCS, and the green and yellow circle pairs represent buckled surface dimers (larger circles represent buckling up and smaller, buckling down).

The interaction between ADCSs and the surface dimers manifests itself in a couple of ways. First, the chain structures disrupt the phase of the buckling of the underlying substrate dimer rows. As mentioned earlier, these chain structures induce localized $c(4\times2)$ pinning of the substrate dimers. This gives rise to an anti-phase boundary in which the registry of the buckling becomes out of phase 180° with that of the substrate dimers on the other side of a C-dimer (see Figures 3-5 and 3-9). This phenomenon has also been observed for similar Si and Ge chain structures on Si(001) and Ge(001) surfaces (in every combination) [33,42–46]. Second, dimer-substrate coupling is clearly seen in STM movies of ADCS dynamics taken at elevated temperatures. The surrounding substrate dimers change their buckling in accord with ADCS rearrangement. This so-called "diffusion driven concerted motion of substrate atoms" was studied for Ge on Ge(001) by Zandvliet *et al.* [42] It was found that this is a natural consequence of the locally induced $c(4\times2)$ buckling of the substrate dimers. These features highlight the interdependence between ADCS motion and the

substrate itself. Thus, ADCSs are not loosely-bound adspecies free to diffuse about the surface; rather, their motion is intimately related to the structure of the substrate.

3.5 *Kink-to-straight ratio of ADCSs*

Another characteristic feature of ADCSs is their observed kink-to-straight ratio. This ratio is defined as the total number of observed kinked addimers to the total number of observed straight addimers at a particular substrate temperature. Analysis of ~8000 ADCSs within the temperature range of 90–150 °C resulted in an experimentally-observed ratio of ~2:1. This ratio indicates that the kinked orientation is energetically favored to the straight configuration by 17 ± 4 meV. In comparison, the configurational preference is exactly reversed for the Ge on Ge(001) system studied by Galea *et al*. [43], wherein they observed similar chain structures to predominantly occupy a more linear, straight configuration, with a corresponding free energy difference of 21 meV.

Given these disparate results for the preference of kinked vs. straight orientations for chain structures, we investigated to what extent entropy is involved. For a 'free' chain structure subjected only to the constraint of maintaining continuity while extending along equivalent ⟨130⟩ directions, we determined the relative number of kinks and straights for all possible *unique* chain configurations. As an example, for the five-unit chain structure shown in Figure 3-10, there are six unique orientations possible—all others are degenerate and related through symmetry operations. There are a total of 9 kinks and 9 straights, for a ratio of 1:1. This exercise was performed with chain structures ranging in length from two units up to seven. (We stopped at seven units, which has 20 unique configurations, as the number of unique configurations increases exponentially with chain length.) For each case, the number of kinks exactly balances the number of straights; so, if

the configurations of ADCSs were completely random, and thus equally favored, one would expect an observed ratio that approaches 1:1. From these observations we conclude that the observed ratio of ~2:1 is not a consequence related to the entropy of ADCSs.

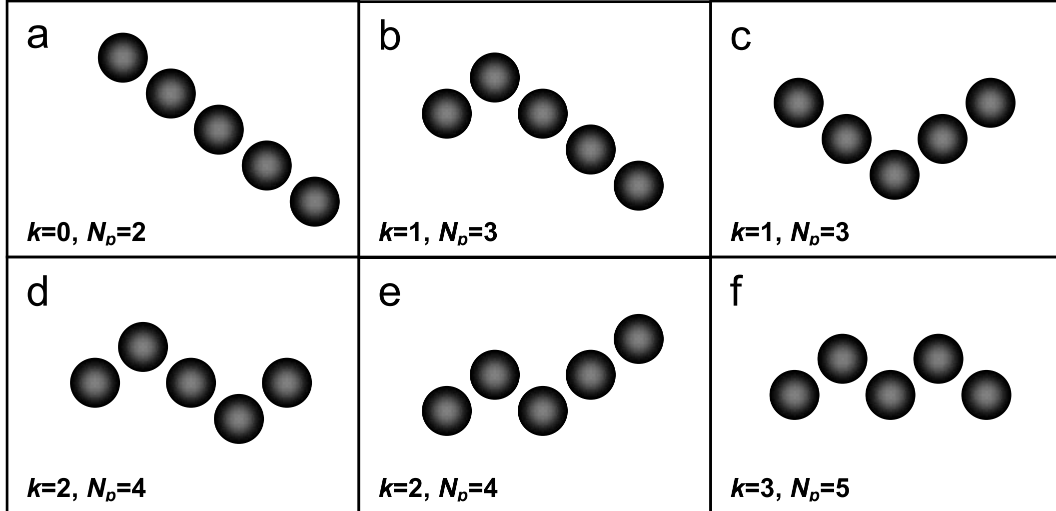

Figure 3-10. **Schematic illustrating the number of unique configurations for a five-unit ADCS.** The ratio of kinks to straights for all of the unique configurations is 1:1. The number of potentially mobile units Np in an ADCS increases with the number of kinks as $N_p=k+2$.

According the 'rules' we observe regarding chain dynamics in Section 3.4, only two dimers are free to move from a completely straight chain configuration [Figure 3-10(a)]: the two end dimers. Alternatively, within a completely kinked chain, *any* of the dimers are able to move [Figure 3-10(f)]. So as the number of kinks k in an ADCS increases, the potential number of moves by constituent C-dimers N_p increases as $N_p=k+2$. Thus, larger numbers of kinks increase the degrees of freedom for an ADCS to move. These degrees of freedom coupled with the tendency to maintain ADCS continuity, enable ADCSs to move back-and-forth between the dimer vacancy lines of the $2\times n$ reconstruction. Thus, to investigate whether confinement of the ADCSs between the DVLs is responsible for the preference of kinks, we performed Monte Carlo simulations of ADCS dynamics. We varied the length of the ADCSs and the value of n for the $2\times n$ structure—i.e., the spacing between the vacancy lines. The chain was allowed to reconfigure according to the relevant

rules (i.e., double-jump diffusion of constituent addimers and preservation of ⟨130⟩ orientations after rearrangement of the chain). Only for the unphysical case of very tight confinement ($n \leq 4$) *and* very long chain lengths did the resulting kink-to-straight ratio approach the observed value of 2:1. Therefore, the free energy difference between the kinked and straight segments of the dimer chains must predominantly be due to a difference in configuration energy.

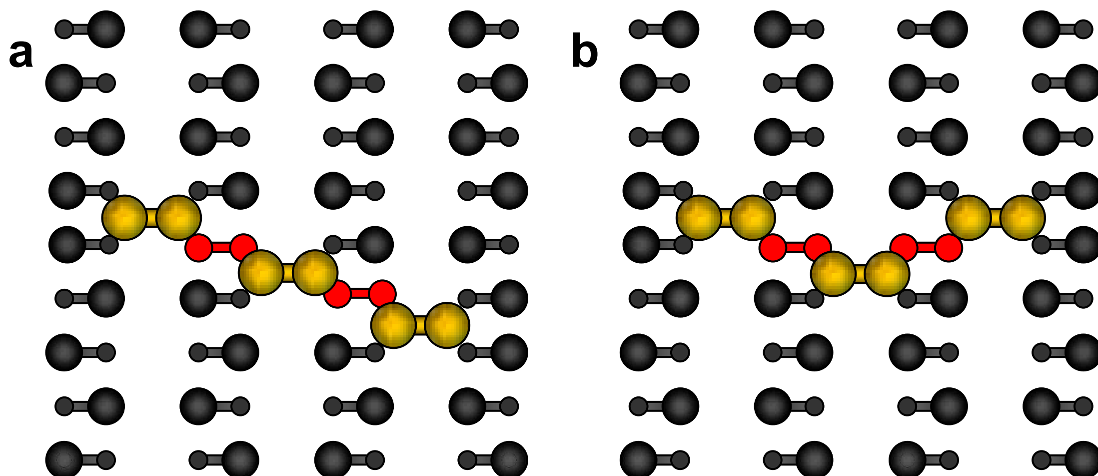

Figure 3-11. **Schematic illustrating configurational ordering of unbuckled substrate dimers (red) in relation to the ADCS orientation kinks vs. straight (gold).** The sizes and grayscale indicate relative heights: features closer to the viewer are larger and lighter gray. (a) ADCS in a straight orientation result in the unbuckled substrate dimers in a ⟨130⟩ direction. (b) A kinked ADCS results in the unbuckled substrate dimers in a ⟨110⟩ direction, which is possibly energetically favorable. The change in buckling registry along the dimer rows induced by ADCS is clearly seen as a natural consequence of the induced in phase buckling of surface dimers due to addimer adsorption.

We speculate that the difference in configuration energy is due to the observed interaction between ADCSs and the arrangements of the underlying substrate dimers, and thus responsible for the preference for kinks. Recall that adsorption of a Ge atom on a Si(001) surface at the M-site induces in-phase buckling of neighboring surface dimers, with the down atoms nearest the adsorbed Ge as in the schematic in Figure 3-6 [56]. Moreover, the anti-phase boundary observed in the substrate dimer buckling caused by ADCSs (see Figures 3-5 and 3-9) is a natural consequence of Ge

binding in the down positions of buckled substrate dimers. Given these characteristics, consider the three-unit ADCSs in Figure 3-11. There are only two unique orientations possible for a three-unit ADCS: completely straight [Figure 3-11(a)], and a kinked, chevron structure [Figure 3-11(b)]. The effect of two neighboring C-dimers in an ADCS is to straighten out one of the surface dimers between them (red dimers). The placement of the third C-dimer in relation to the other two affects the ordering of these unbuckled substrate dimers. For example, the ADCS in Figure 3-11(a) results in the unbuckled substrate dimers being offset from each other by one lattice site in a ⟨130⟩ direction. Conversely, the kinked ADCS in Figure 3-11(b), positions the two unbuckled substrate dimers in line with each other along a ⟨110⟩ direction. Thus, it is possible that there is an energetic advantage to maintaining the alignment of unbuckled substrate dimers along a ⟨110⟩ orientation as opposed to being offset, much in the same way that kinks in DVLs [74–76] and step edges [77,78] cost energy.

3.6 *Transition of ADCSs to compact epitaxial islands*

We have observed that these 'diluted' ADCSs transition to more stable compact epitaxial islands at elevated temperatures. Figure 3-12 shows filled- and empty-state images of a six-unit ADCS before and after conversion to CEI segments. The chain structure is characteristically only seen in the empty-state image [Figure 3-12(b)]. However, after the ADCS converts into two compact epitaxial segments, these islands are easily seen in both polarities [Figures 3-12(c) and (d)]. Because the conversion to compact epitaxial islands is a thermally-activated process, we measure the conversion rate as a function of temperature to calculate the associated activation energy and pre-exponential factor. The populations of both ADCSs and CEIs are monitored with respect to time over a range of temperatures (90–150 °C).

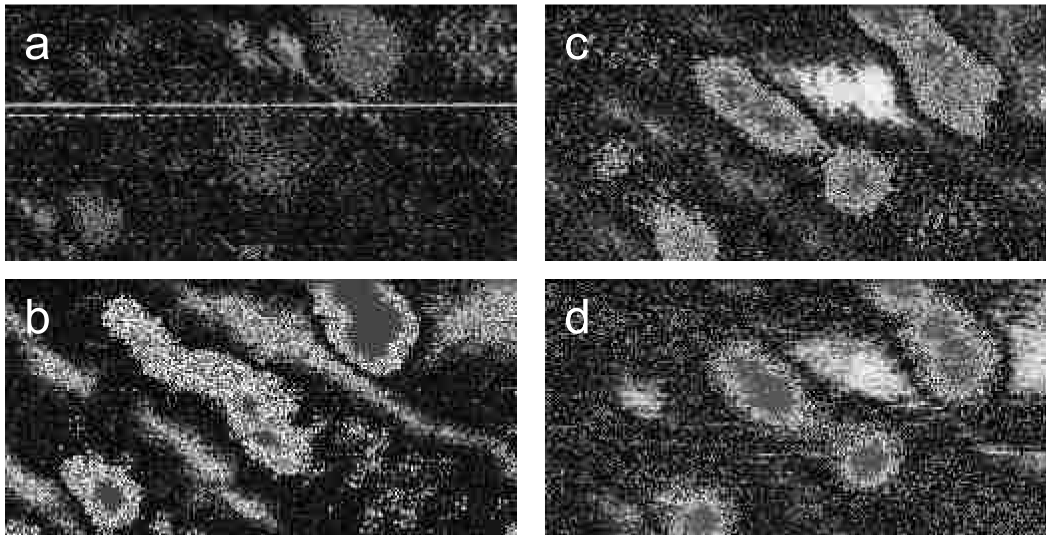

Figure 3-12. **Filled- and empty-state STM images showing an ADCS before and after its transition to a compact island.** (a) Filled states (+1.7 V) before (b) empty states (–1.7 V) before (c) filled states after and (d) empty states after. Notice the surrounding epitaxial islands are visible in both biases before and after.

We implemented a digital image-processing algorithm in order to extract the ADCS and compact island population distributions from STM images. The algorithm can be summarized by three key steps†: First, the height difference between neighboring terraces on the surface (separated by monatomic steps) results in a contrast variation in the grayscale intensity for adspecies on different terraces. A combination of filtering techniques is used to negate this height difference effect as well as to enhance adspecies contrast relative to the surface [79,80]. Second, a mask is created to isolate all of the adspecies on the surface (ADCSs and compact islands), yielding binary filled- and empty-state images [80]. Finally, a classification step is performed to discriminate between ADCSs and compact islands [80]. This is accomplished by employing the fact that ADCSs only appear in empty-state images, while compact islands appear in filled- *and* empty-states.

By plotting the normalized areas of ADCSs, in pixels, as a function of time, the population decay of ADCSs—due to transition to compact islands—is obtained for a variety of temperatures.

† For a more detailed description of the image processing algorithm and processed images, see Appendix.

From the temporal population decay of ADCSs, we extract a characteristic decay time, τ, for each temperature from a first-order exponential decay model (see Figure 3-13).

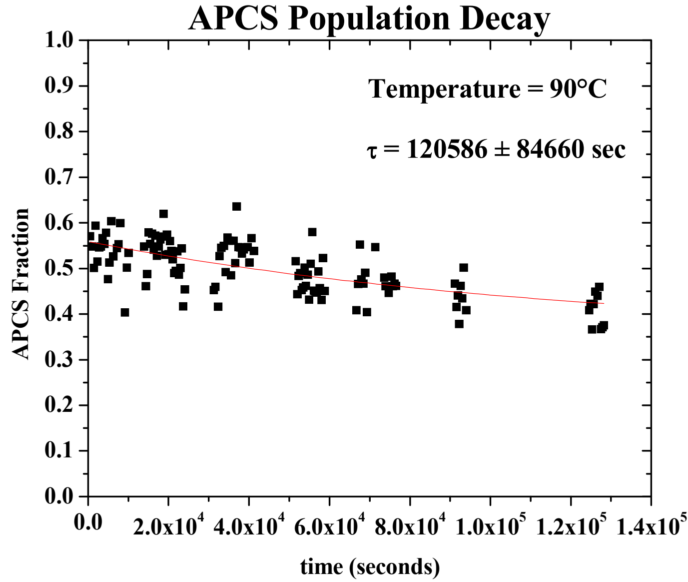

Figure 3-13. **Typical temporal ADCS population decay data with associated time constant.** Conversion data for 90 °C shown.

Each data point in Figure 3-13 is based on a 500 Å × 500 Å STM image. The total number of data points for each temperature ranges from about ten for the highest substrate temperature, to 100 for the lowest. We note that not all ADCSs covert to compact epitaxial islands, resulting in a finite population of unconverted mass. We speculate that the incomplete conversion is caused by the presence of defects, which can stabilize some of the ADCSs and prevent their transition to compact islands. The temperature-dependent decay times are then fit to a classical Arrhenius-type expression, from which the relevant kinetic values are extracted. From Figure 3-14, we compute the activation energy E_a associated with the transition of ADCSs to compact islands as 0.7 ± 0.2 eV with a pre-exponential factor ν_0 of the order of $5 \times 10^{4\pm2}$ s^{-1}.

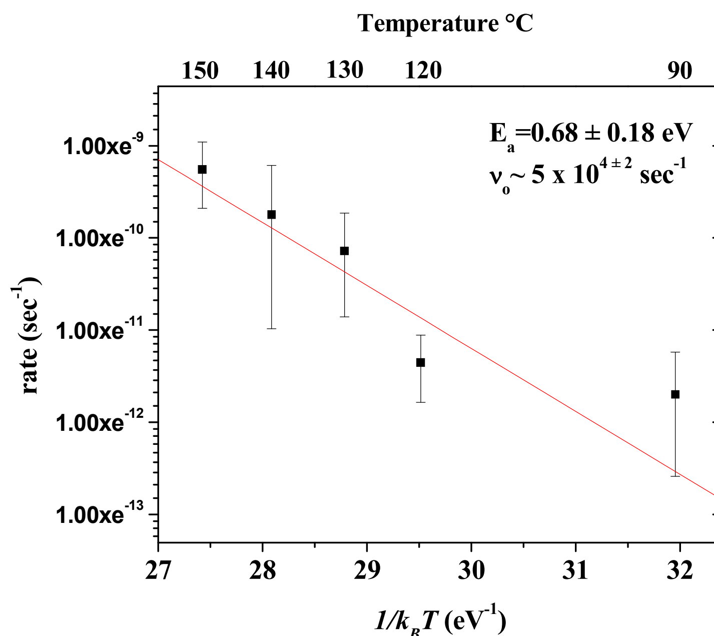

Figure 3-14. Arrhenius plot for 90°C < T < 150°C showing activation energy and pre-exponential factor associated with ADCS-island transition.

The activation energy we computed for the conversion of ADCSs to CEIs is comparable to that for adatom diffusion [28,51–57]. Such an activation energy would imply that, at room temperature, the conversion rate is $\sim 10^5$ times faster than for typical addimer diffusion [36–38,46–50]! However, if this were the case, the conversion rate of ADCSs to CEIs would be so fast that we would not be able to observe ADCSs in any appreciable quantity; and, this would indeed be the case if the prefactor was of the order of $\sim 10^{13}\ s^{-1}$, which is the commonly accepted value for diffusive processes [81]. However, we measure an anomalously low prefactor, by nearly ten orders of magnitude. We surmise that the extremely low prefactor may reflect the possibly complex nature of the conversion mechanism itself. Based on our previous observations, the mechanism is likely multi-bodied, requiring a concerted motion of multiple addimers along with concomitant rearrangements of the substrate dimers. Indeed, a similarly complicated mechanism is predicted

for Si homoepitaxy [82]. Further investigation regarding the origin of the observed low prefactor is needed.

3.7 *Conclusions*

We have identified addimer chain structures (ADCSs) as metastable precursors to the formation of compact epitaxial islands on the Ge-Si(001)-(2×*n*) alloy wetting layer. ADCSs consist of chains of C-dimers residing in adjacent troughs, extending along all equivalent ⟨130⟩ directions, with chain lengths typically ranging from two to about twelve units. We observe the preferential formation of ADCSs on this surface at room temperature upon sub-monolayer Ge deposition, suggesting their formation is kinetically limited. We propose an Adatom-Trapping-Addition mechanism to explain ADCS formation and growth. The dynamics of ADCSs are intimately related to the underlying surface dimer structure. ADCSs exhibit limited mobility on the surface, and undergo configurational rearrangements while maintaining ⟨130⟩ orientations and chain continuity. These ADCSs exhibit a zigzagged morphology, possessing kinked and straight segments, with an observed kink-to-straight ratio close to 2:1, corresponding to a free energy difference of 17 ± 4 meV. Upon annealing, ADCSs convert to compact islands, with an associated activation energy of 0.7 ± 0.2 eV and an anomalously low attempt frequency of $5 \times 10^{4\pm2}$ s^{-1}. The transition mechanism from ADCSs to CEIs is likely a complicated, multi-bodied process involving addimers and concomitant substrate dimer rearrangement.

3.8 *References*

[1] R.J. Wagner and E. Gulari, *Phys. Rev. B* **69**, 195312 (2004).

[2] R.M. Tromp, *Phys. Rev. B* **47**, 7125 (1992).

[3] B. Voigtländer and M. Kästner, *Phys. Rev. B* **60**, R5121 (1999).

[4] L. Nurminen, F. Tavazza, D.P. Landau, A. Kuronen, and K. Kaski, *Phys. Rev. B* **68** 085326 (2003).

[5] F. Liu, F. Wu, and M.G. Lagally, *Chem. Rev.* **97**, 1045 (1997).

[6] D. Papajová and H. Sitter, *Semicond. Sci. Technol.* **13**, 1247 (1998).

[7] Z. Zhang and M.G. Lagally, *Science* **276**, 377 (1997).

[8] B. Voigtländer, *Surf. Sci. Rep.* **43**, 127 (2001).

[9] M.A. Herman and H. Sitter, *Microelectr. J.* **27**, 257 (1996).

[10] D.K. Goswami, B. Satpati, P.V. Satyam, and B.N. Dev, *Curr. Sci. India* **84**, 903 (2003).

[11] M. Volmer and A. Weber, *Z. Phys. Chem.* **119**, 227 (1926).

[12] F.C. Frank and J.H. van der Merwe, *Proc. Roy. Soc. London A* **198**, 205 (1949).

[13] W.K. Burton, N. Cabrera, and F.C. Frank, *Philos. Trans. R. Soc. London A* **243**, 299 (1951).

[14] G.S. Bales and A. Zangwill, *Phys. Rev. B* **41**, 5500 (1990).

[15] D.J. Eaglesham and M. Cerullo, *Phys. Rev. Lett.* **64**, 1943 (1990).

[16] Y.-W. Mo, D.E. Savage, B.S. Swartzentruber, and M.G. Lagally, *Phys. Rev. Lett.* **65**, 1020 (1990).

[17] I.N. Stranski and L. von Krastanow, *Abhandlungen der Mathematisch-Naturwissenschaftlichen Klasse. Akademie der Wissenschaften und der Literatur in Mainz* **146**, 797 (1939).

[18] R. Butz and S. Kampers, *Appl. Phys. Lett.* **61**, 1307 (1992).

[19] F.-K. Men and C.-R. Hsu, *Phys. Rev. B* **58**, 1130 (1998).

[20] J. Oviedo, D.R. Bowler, and M.J. Gillan, *Surf. Sci.* **515**, 483 (2002).

[21] J. Knall and J.B. Pethica, *Surf. Sci.* **265**, 156 (1992).

[22] U. Köhler, O. Jusko, B. Müller, M.Horn-von Hoegen, and M. Pook, *Ultramicroscopy* **42–44**, 832 (1992).

[23] M. Tomitori, K. Watanabe, M. Kobayashi, and O. Nishikawa, *Appl. Surf. Sci.* **76–77**, 322 (1994).

[24] M.J. Beck, A. van de Walle, and M. Asta, *Phys. Rev. B* **70**, 205337 (2004).

[25] G. Medeiros-Ribeiro, A.M. Bratkovski, T.I. Kamins, D.A.A. Ohlberg, and R. Stanley Williams, *Science* **279**, 353 (1998).

[26] J.A. Floro, E. Chason, L.B. Freund, R.D. Twesten, R.Q. Hwang, and G.A. Lucadamo, *Phys. Rev. B* **59**, 1990 (1999).

[27] F.M. Ross, R.M. Tromp, and M.C. Reuter, *Science* **286**, 1931 (1999).

[28] G. Brocks, P.J. Kelly, and R. Car, *Surf. Sci.* **269–270**, 860 (1992).

[29] Z. Zhang, F. Wu, H.J.W. Zandvliet, B. Poelsema, H. Metiu, and M.G. Lagally, *Phys. Rev. Lett.* 74, 3644 (1995).

[30] B.S. Swartzentruber, A.P. Smith, and H. Jónsson, *Phys. Rev. Lett.* **77**, 2518 (1996).

[31] T. Yamasaki, T. Uda, and K. Terakura, *Phys. Rev. Lett.* **76**, 2949 (1996).

[32] G. Brocks and P.J. Kelly, *Phys. Rev. Lett.* **76**, 2362 (1996).

[33] J. van Wingerden, A. van Dam, M.J. Haye, P.M.L.O. Scholte, and F. Tuinstra, *Phys. Rev. B* **55**, 4723 (1997).

[34] A. van Dam, J. van Wingerden, M.J. Haye, P.M.L.O. Scholte, and F. Tuinstra, *Phys. Rev. B* **54**, 1557 (1996).

[35] P.J. Bedrossian, *Phys. Rev. Lett.* **74**, 3648 (1995).

[36] B. Borovsky, M. Krueger, and E. Ganz, *Phys. Rev. Lett.* **78**, 4229 (1997).

[37] A.P. Smith and H. Jónsson, *Phys. Rev. Lett.* **77**, 1326 (1996).

[38] Y.-W. Mo, R. Kariotis, B.S. Swartzentruber, M.B. Webb, and M.G. Lagally, *J. Vac. Sci. Technol. A* **8**, 201 (1990).

[39] R.J. Hamers, R.M. Tromp, and J.E. Demuth, *Phys. Rev. B* **34**, 5343 (1986).

[40] R.A. Wolkow, *Phys. Rev. Lett.* **68**, 2636 (1992).

[41] H. Tochihara, T. Amakusa, and M. Iwatsuki, *Phys. Rev. B* **50**, 12262 (1994).

[42] H.J.W. Zandvliet, T.M. Galea, E. Zoethout, and B. Poelsema, *Phys. Rev. Lett.* **84**, 1523 (2000).

[43] T.M. Galea, C. Ordas, E. Zoethout, H.J.W. Zandvliet, and B. Poelsema, *Phys. Rev. B* **62**, 7206 (2000).

[44] S. Liu, C.S. Jayanthi, S.-Y. Wu, X. Qin, Z. Zhang, and M.G. Lagally, *Phys. Rev. B* **61**, 4421 (2000).

[45] X.R. Qin and M.G. Lagally, *Science* **278**, 1444 (1997).

[46] W. Wulfhekel, B.J. Hattink, H.J.W. Zandvliet, G. Rosenfeld, and B. Poelsema, *Phys. Rev. Lett.* **79**, 2494 (1997).

[47] B.S. Swartzentruber, *Phys. Rev. Lett.* **76**, 459 (1996).

[48] M. Krueger, B. Borovsky, and E. Ganz, *Surf. Sci.* **385**, 146 (1997).

[49] E. Zoethout, H.J.W. Zandvliet, W. Wulfhekel, G. Rosenfeld, and B. Poelsema, *Phys. Rev. B* **58**, 16167 (1998).

[50] X.R. Qin, B.S. Swartzentruber, and M.G. Lagally, *Phys. Rev. Lett.* **85**, 3660 (2000).

[51] Y.-W. Mo, B.S. Swartzentruber, R. Kariotis, M.B. Webb, and M.G. Lagally, *Phys. Rev. Lett.* **63**, 2393 (1989).

[52] G. Brocks, P.J. Kelly, and R. Car, *Phys. Rev. Lett.* **66**, 1729 (1991).

[53] Y.-W. Mo and M.G. Lagally, *Surf. Sci.* **248**, 313 (1991).

[54] Y.-W. Mo, J. Kleiner, M.B. Webb, and M.G. Lagally, *Phys. Rev. Lett.* **66**, 1998 (1991).

[55] C. Roland and G.H. Gilmer, *Phys. Rev. B* **46**, 13428 (1992).

[56] V. Milman, D.E. Jesson, S.J. Pennycook, M.C. Payne, M.H. Lee, and I. Stich, *Phys. Rev. B* **50**, 2663 (1994).

[57] A.P. Smith, J.K. Wiggs, H. Jónsson, H. Yan, L.R. Corrales, P. Nachtigall, and K.D. Jordan, *J. Chem. Phys.* **102**, 1044 (1995).

[58] R.A. Wolkow, *Phys. Rev. Lett.* **74**, 4448 (1995).

[59] B.S. Swartzentruber, *Phys. Rev. B* **55**, 1322 (1997).

[60] C. Roland and G.H. Gilmer, *Phys. Rev. Lett.* **67**, 3188 (1991).

[61] Z. Zhang, Y.-T. Lu, and H. Metiu, *Phys. Rev. B* **46**, 1917 (1992).

[62] D. Srivastava and B.J. Garrison, *Phys. Rev. B* **47**, 4464 (1993).

[63] Q.-M. Zhang, C. Roland, P. Boguslawski, and J. Bernholc, *Phys. Rev. Lett.* **75**, 101 (1995).

[64] J. Wang, D.A. Drabold, and A. Rockett, *Surf. Sci.* **344**, 251 (1995).

[65] E. Zoethout, H.J.W. Zandvliet, and B. Poelsema, *J. Vac. Sci. Technol. A* **19**, 1868 (2001).

[66] G. Brocks, P.J. Kelly, and R. Car, *Phys. Rev. Lett.* **70**, 2786 (1993).

[67] J. Wang and A. Rockett, *Phys. Rev. B* **43**, 12571 (1991).

[68] Z.-Y. Zhang, Y.-T. Lu, and H. Metiu, *Surf. Sci.* **248**, L250 (1991).

[69] Y.-T. Lu, Z.-Y. Zhang, and H. Metiu, *Surf. Sci.* **257**, 199 (1991).

[70] Y.-W. Mo, J. Kleiner, M.B. Webb, and M.G. Lagally, *Surf. Sci.* **268**, 275 (1992).

[71] X.R. Qin, F. Liu, B.S. Swartzentruber, and M.G. Lagally, *Phys. Rev. Lett.* **81**, 2288 (1998).

[72] R.V. Kukta, D. Kouris, and K. Sieradzki, *J. Mech. Phys. Solids* **51**, 1243 (2003).

[73] R.V. Kukta, P. Liu, and D. Kouris, *J. Mech. Phys. Solids* **51**, 2149 (2003).

[74] X. Chen, F. Wu, Z. Zhang, and M.G. Lagally, *Phys. Rev. Lett.* **73**, 850 (1994).

[75] F.-K. Men, A.R. Smith, K.-J. Chao, Z. Zhang, and C.-K. Shih, *Phys. Rev. B* **52**, R8650 (1995).

[76] C.V. Ciobanu, D. T. Tambe, and V. B. Shenoy, *Surf. Sci.* **556**, 171 (2004).

[77] D.J. Chadi, *Phys. Rev. Lett.* **59**, 1691 (1987).

[78] B.S. Swartzentruber, Y.-W. Mo, R. Kariotis, M.G. Lagally, and M.B. Webb, *Phys. Rev. Lett.* **65**, 1913 (1990).

[79] P. Viola and W.M. Wells, *Int. J. Comput. Vision* **24**, 137 (1997).

[80] K.R. Castleman, *Digital Image Processing*, (Prentice Hall, Upper Saddle River, 1996).

[81] G.L. Kellogg, *Surf. Sci. Rep.* **21**, 1 (1994).

[82] S. Dağ, S. Ciraci, Ç. Kılıç, and C.Y. Fong, *Surf. Sci.* **479**, 109 (2001).

Chapter 4

Scanning tunneling spectroscopy of the SiGe alloy wetting layer

During epitaxy, the surface serves as the "template" for further growth, so surface characteristics such as reconstruction and defects are important. In the case of alloys, growth may also be affected by the structure or compositional ordering at the surface; which in turn are largely determined by the growth kinetics, especially in the case of strained heteroepitaxy (e.g., SiGe) [1]. Moreover, many metallic alloy systems (e.g., PtNi, PbCu) display varying degrees of compositional ordering [2–4]; thus, it seems possible that the SiGe alloy may as well. Specifically, we desire to understand how the two elements interact, mix, and assemble during epitaxy, and whether the resultant alloy structure is ordered or disordered. Such information will provide a more complete understanding of the early stages of heteroepitaxy of Ge on Si(001).

Central to the understanding of compositional ordering and structure of an alloy surface, is the ability to achieve chemical contrast on an atomic scale [2]. Achieving chemical contrast between Si and Ge has been considered difficult, if at all possible, because of their *similar* properties (e.g., atomic, electronic, and chemical). However, it is precisely their *differences* in these properties that we shall attempt to exploit. Toward this end, a series of preliminary scanning tunneling spectroscopy investigations on SiGe alloy surfaces of various compositions was carried out. The particular techniques used were low-bias empty-state STM imaging, polarity-switching STM, and scanning tunneling spectroscopy (STS). The details regarding these techniques are addressed in Chapter 2.

4.1 *Si(001)-(2×1) surface*

The STM relies on the quantum-mechanical tunneling current between the surface and probe to map the surface. Recall from Chapter 2 that the tunneling current is a function of the local density of (electronic) states (LDOS) *and* depends exponentially on the tip-sample separation. Thus, both *electronic* and *physical* information about the surface (and probe tip) are intrinsically convolved in the tunneling current, and therefore images. Moreover, this convolution often can prove difficult in resolving and interpreting the contributions due to electronic structure versus topographic features. The clean Si(001)-(2×1) surface is a prime example of the convolution of topographic and electronic data; and as such, its geometric [5–11] and electronic [12–23] structures have been extensively investigated both theoretically and experimentally.

It is now well known that the Si(001) bulk terminated surface reconstructs in a 2×1 fashion, wherein each Si surface atom covalently bonds with one of its surface neighbors. This reconstruction reduces the number of dangling bonds by a factor of two, and thusly the free energy of the surface. The resulting pair-bonded surface atoms (dimers) align into rows, as shown in Figure 4-1. These *dimer rows* extend perpendicular to the dimer bond direction. A collection of parallel dimer rows that comprise the surface atomic layer is called a *terrace*. The orientation of the dimer bond, and hence the orientation of dimer rows, rotates 90° from one terrace (2×1) to another (1×2). Adjacent terraces are separated by a monatomic step. This alternating arrangement of dimer rows between adjacent terraces is a direct result of the diamond cubic crystal structure of silicon.

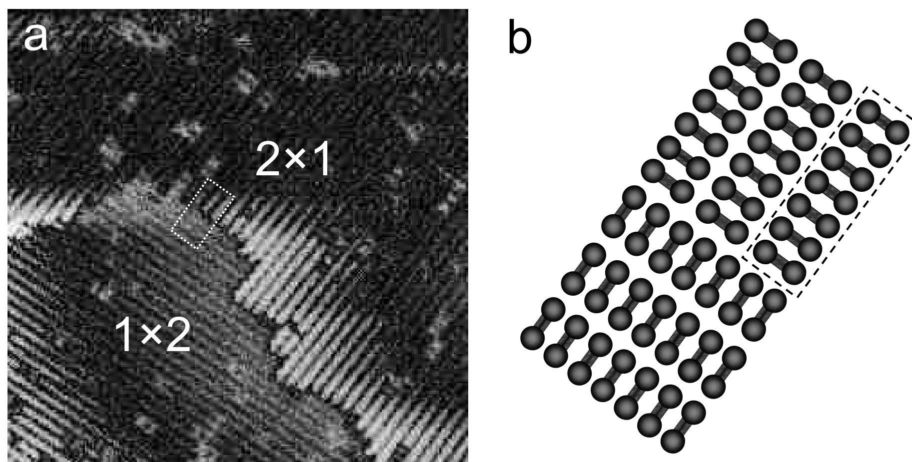

Figure 4-1. Si(001)-(2×1) surface. (a) STM image of a Si(001)-(2×1) surface. Two terraces are visible in which the direction of the dimer bonds (and dimer rows) is rotated by 90° with respect to each other. (b) The section outlined by a white dotted rectangle in (a) is represented by an enlarged schematic with a section of a dimer row outlined by a dashed rectangle. Dimer rows extend perpendicular to the dimer bond direction.

The STM images of the clean Si(001)-(2×1) surface are dominated by the surface electronic structure [14]. For example, Figure 4-2 demonstrates that images of the filled and empty electronic states have different spatial distributions within the 2×1 unit cell (white rectangle). In the filled-state image [Figure 4-2(a)], a dimer appears as a bean-shaped object with a single maximum, which corresponds to the π-bonding orbital. Conversely, the empty-state image [Figure 4-2(b)] shows two circular maxima (π^*-antibonding orbitals) separated by a dark minimum in the center. This minimum corresponds to the existence of a node in the antisymmetric wavefunctions of the antibonding orbitals, as corroborated by the calculated electronic structure of this surface [5,6,15]. In this way, STM images of the paired-atom *structural* arrangement of surface dimers visually reflect the symmetry in the *electronic* surface-state wavefunctions of bonding/antibonding orbitals.

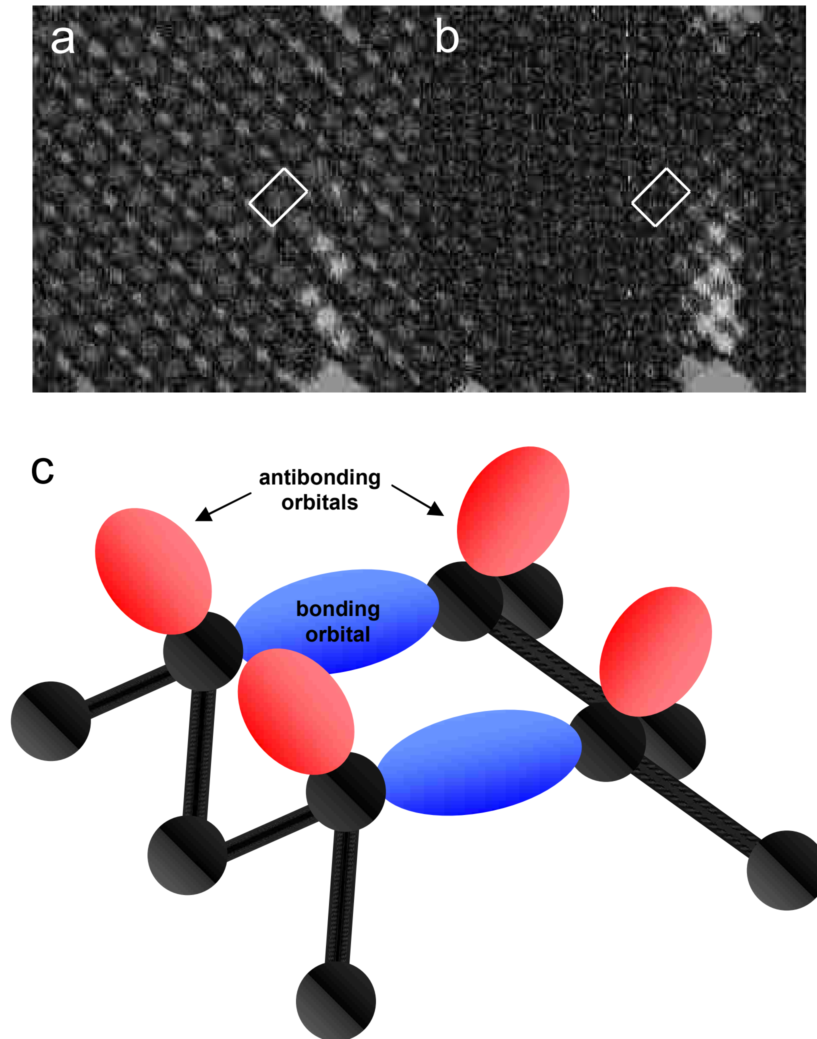

Figure 4-2. Physical and electronic structure of Si(001)–(2×1) reconstruction. (a) Filled-state image (−1.7 V) and (b) empty-state image (+2.0 V). A 2×1 unit cell, corresponding to an individual surface dimer, is outlined with a white rectangle. In the filled state image, dimers appear as symmetric, bean-shaped objects, whereas the empty-state image shows two distinct maxima per unit cell. (c) The model illustrates two Si surface dimers (light gray circles) bonded to silicon atoms in the atomic layer below (dark gray circles). The bonding orbitals (blue) are regions of high electron density and correspond to the bean-shaped dimers in filled state images. Additionally, each surface Si atom possesses a single dangling bond/antibonding orbital (red), which shows as a circle in the empty-state images.

The pristine Si(001)–(2×1) surface is an idealization, and is generally vulnerable to a variety of missing dimer defects [7–9,17]. Figure 4-3 shows filled- (a) and empty-state (b) STM images of a Si(001)–(2×1) surface displaying a variety of common defects, which appear as black holes in the dimer rows: *Type A* defects are those in which a single dimer is missing from the

surface; *Type B* defects occur when two adjacent surface dimers are missing from the same row; and *Type C* defects result from two adjacent dimers in the same row missing the same half of each dimer. These latter defects are typically due to adsorbates, and are easily seen as bright blobs in the empty-state image that occupy the opposite side of the dimer row as the defect. Additionally, a commonly observed composite defect known as a *two-plus-one*, is a Type A defect separated by one dimer from a Type B defect on the same dimer row.

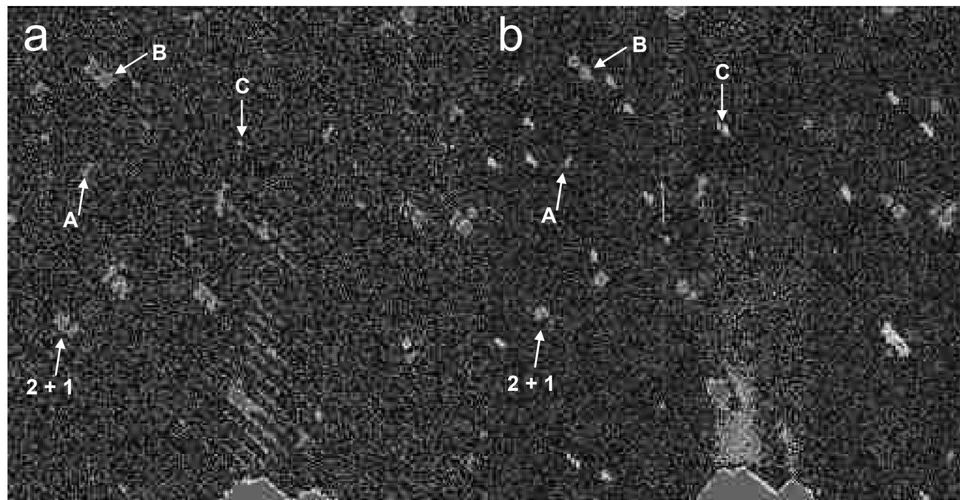

Figure 4-3. Commonly observed surface defects on Si(001)-(2×1). (a) Filled- and (b) empty-state images of a Si(001)-(2×1) surface displaying a variety of surface defects. Defects generally appear as black holes due to dimers missing from the surface. Most of the defects have a similar appearance in both biases, although Type C defects are associated with adsorption of impurities, which show as bright blobs in empty-state images but are invisible in filled-state images.

The above-mentioned defects can alter the (2×1) structure of surrounding surface dimers. At room temperature, surface dimers oscillate in and out of the surface plane about their centers of mass (like seesaws) at a frequency much faster than the response time of the STM. Such *dynamic buckling* causes the surface dimers to appear symmetric and bean-shaped in filled-state STM images [8,9,19]. However, defect-induced pinning can cause surface dimers to become *statically* buckled, and thus appear asymmetrical [8,9].

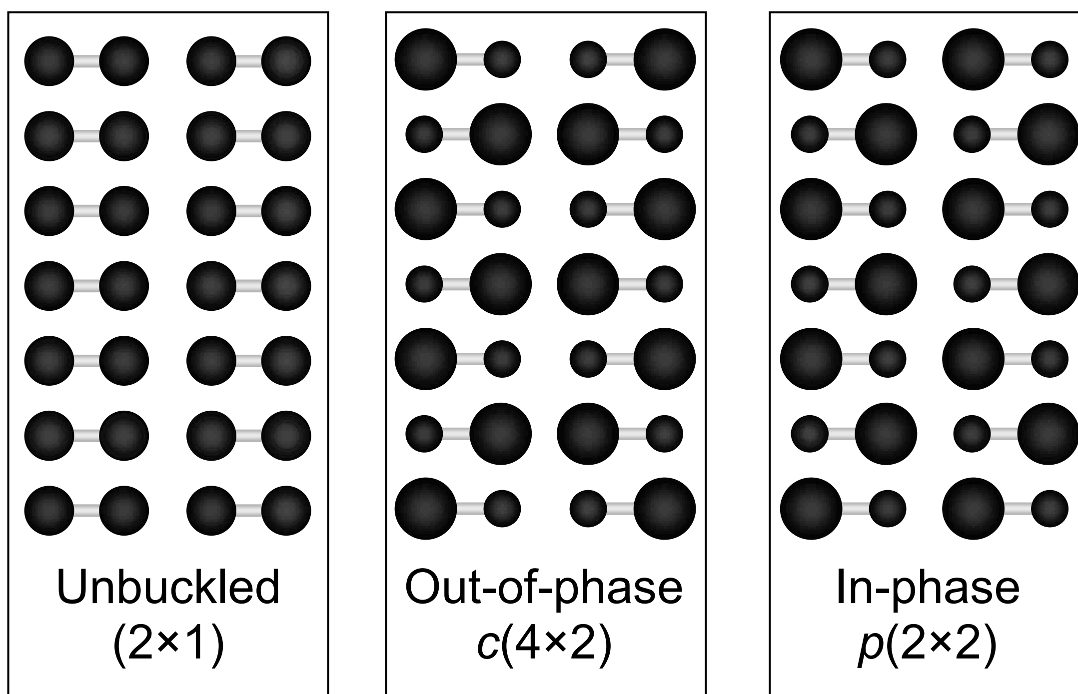

Figure 4-4. Three common surface reconstructions for Si(001). Large dots represent atoms buckled out of the surface plane and closer to the reader, whereas smaller dots are buckled into the plane away from the reader. In STM images, areas of $c(4\times2)$ buckling appear honeycomb-like, and regions of $p(2\times2)$ are zigzagged.

These statically buckled dimers can arrange to form two different phases of higher order reconstruction, illustrated in Figure 4-4: (1) an out-of-phase $c(4\times2)$ reconstruction, wherein the buckling of adjacent dimer rows are mirror images of each other, or (2) an in-phase $p(2\times2)$ reconstruction, wherein the buckling of adjacent dimer rows is exactly the same. All of these surface irregularities (i.e., defects and buckling) can affect the diffusion and nucleation of deposited adspecies.

We now consider the electronic structure of a silicon surface similar to the one in Figure 4-1 by scanning tunneling spectroscopy (STS). In addition to the filled- and empty-state STM topographs, we include the corresponding STS conductance images. A detailed description of the STS technique is included in Chapter 2. Briefly, STS generates a conductance image of the surface, corresponding to same spatial area scanned as the STM topograph. A conductance image indicates

the spatial dependence of the differential conductance (*dI/dV*) of the surface at a constant dc applied bias voltage. The conductance approximates the LDOS of the surface, so a large conductance corresponds to a high DOS at particular energy (bias voltage). As the STM topograph is a grayscale image depicting surface topography (white higher, black lower), the STS conductance image shows regions of high conductance (white) and low conductance (black).

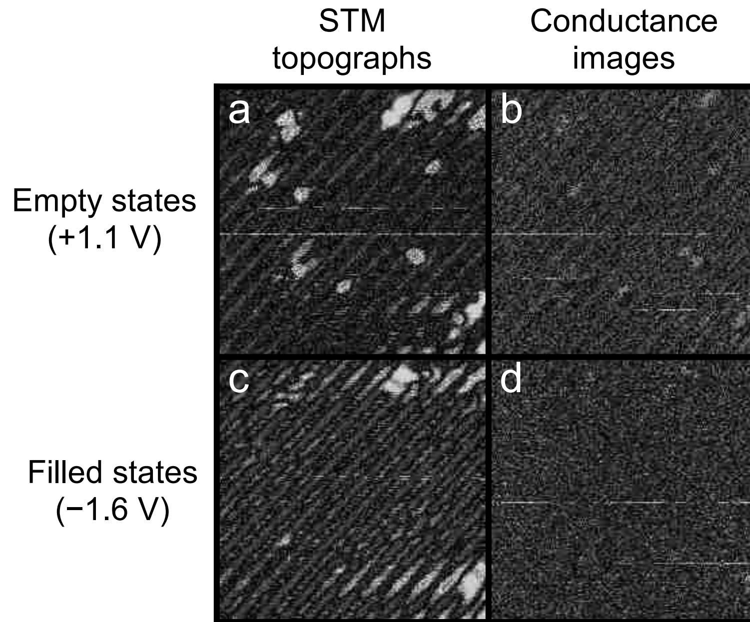

Figure 4-5. STS of Si(001)-(2×1). STM topographs of empty- (a) and filled-states (c) with corresponding conductance images for each bias (b) filled and (d) empty. Notice the dark lines in the STM topographs are shifted by 90° between filled- and empty-states. Type C defects are visible as bright blobs in the empty-state STM image and change contrast in the corresponding conductance image.

Figure 4-5 shows STM topographs and STS conductance images for filled- and empty-states for a Si(001) surface. First, the positions of the dark lines in the empty-state STM image are shifted 90° with respect to those in the filled-state STM image, easily seen by the relative position of the large surface defect at the top right of the images. This shift is a manifestation of the spatial distribution of electronic states as discussed above in reference to Figure 4-2. Type C defects are also visible with the characteristic bright blob signatures in the empty-state STM image due to the

presence of adsorbates. The empty-state conductance image shows these features as dark spots, whereas they appear as faint bright spots in the filled-state conductance image.

4.2 *$Si_{1-x}Ge_x$ alloy wetting layer*

To investigate the $Si_{1-x}Ge_x$ alloy surface, a graded approach was taken to incrementally increase the Ge content, x, in the silicon surface up to a fully-developed SiGe ($2\times n$) wetting layer. Discrete Ge compositions of 0.04, 0.10, 0.25, 0.5, and 1.5 monolayers (ML) were then investigated. In this manner, we expect that any observable changes in the data can be tracked and attributed to the increasing Ge content of the alloy surface. The depositions were performed at a growth temperature of about 550 °C to allow for a substantial amount of intermixing of the Ge with the Si substrate.

We first investigated a low-Ge-composition SiGe surface corresponding to 0.04 ML of Ge deposited. Even at such a small Ge content, a number of differences in the surface arise as compared with clean Si(001). First, in the filled-state STM image [Figure 4-6(a)], much of the surface is statically buckled in $c(4\times2)$ and $p(2\times2)$ phases instead of rows of symmetric bean-shaped dimers. This buckling is caused by larger Ge intermixing with substrate Si [24]. In fact, low-bias, empty-state imaging [Figure 4-6(b)] clearly shows bright regions in the vicinity of the buckling, which correspond to intermixed Ge. One such region is highlighted by the white rectangle. Moreover, the observed buckling arrangement in the empty-state image is a mirror image of the filled-states [22,25].

The apparent antisymmetric buckling (mirror image) between filled- and empty-state images is understood by considering the details of Ge intermixing into the Si(001) surface. For instance, at low Ge compositions, mixed SiGe dimers are known to preferentially form [26–30].

Furthermore, due to the larger size of Ge compared with Si, it is energetically favorable for the mixed dimer to buckle or tilt out of the surface plane to relieve stress, with Ge in the ‘up’ position and Si in the ‘down’ position [27–29]. The tilt angle of mixed SiGe dimers is larger [29–32] than that of Si surface dimers in either $c(4\times2)$ or $p(2\times2)$ regions [33]. This buckled orientation, coupled with the slightly larger electronegativity of Ge over Si, induces charge transfer of electron density from the down Si to the up Ge, causing the bond to become semi-ionic [21,24,27,34]. (Similar charge transfer occurs within buckled dimers in Si(001) [6,10,12,14,35–37], Ge(001) [25,38], and GaAs(110) [39] surfaces.) Because this charge transfer shifts electron density from Si to Ge, filled-state imaging—in which tunneling electrons are conducting from the surface to the tip—shows Ge as a protrusion, due to its larger contribution to the tunneling current. Conversely, in empty-state imaging, electron-depleted Si can accept more tunneling current than Ge; thus, the protrusion now occurs over Si, causing the apparent buckling shift. This effect is illustrated in Figure 4-6(c)-(d) by the differing STM tip trajectories over a buckled SiGe dimer for filled- and empty-state imaging.

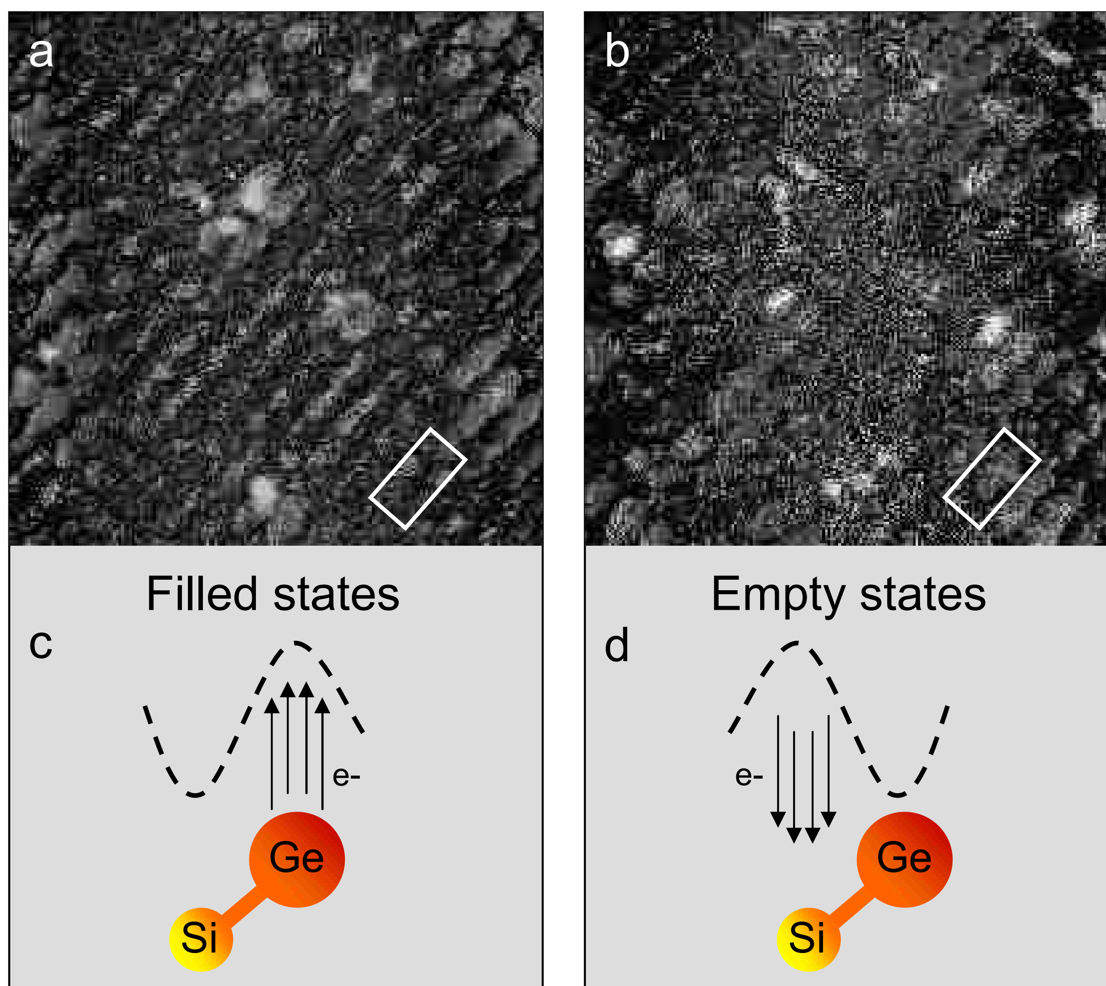

Figure 4-6. Buckling and charge transfer in mixed SiGe dimers. (a) Filled- (–0.9 V) and (b) empty-state (+0.9 V) STM images of a Si(001)-(2×1) surface exposed to 0.04 ML Ge. The surface topography displays a large fraction of buckled surface dimers due to Ge intermixing. Ge is easily seen in the empty-state image as the bright regions in the surface. The observed buckling in the empty-state image is opposite that in the filled-state image (white rectangle). (c) and (d) A mixed SiGe dimer buckles with the Ge in the "up" position and the Si in the "down" position. This tilted orientation causes charge transfer from Si to Ge. The STM tip trajectories are shown, illustrating that the images are inverted between (c) filled- and (d) empty-states.

By increasing the magnitude of the sample bias in the same region as in Figure 4-6, another effect becomes apparent. Figure 4-7 compares empty-state images for two different values of bias voltage: Figure 4-7(a) is the empty-state image of Figure 4-6(b) at a sample bias voltage of +0.9 V, and Figure 4-7(b) is an empty-state image of the same region (with slight drift) at +1.4 V. Notice that at higher voltages, at the locations of Ge incorporation [i.e., bright regions in Figure 4-7(a)],

the dimer rows appear to 'neck' or 'pinch off' interrupting the black lines [Figure 4-7(b)], as indicated by the white arrows. This phenomenon is attributed to the delocalization of surface electronic states at higher energies, which is also responsible for the diminished resolution of individual dimers at high-bias voltages in empty-state imaging [22]. Thus, this pinch-off effect serves as a complementary means for highlighting regions of Ge incorporation at higher-bias values in empty-state imaging.

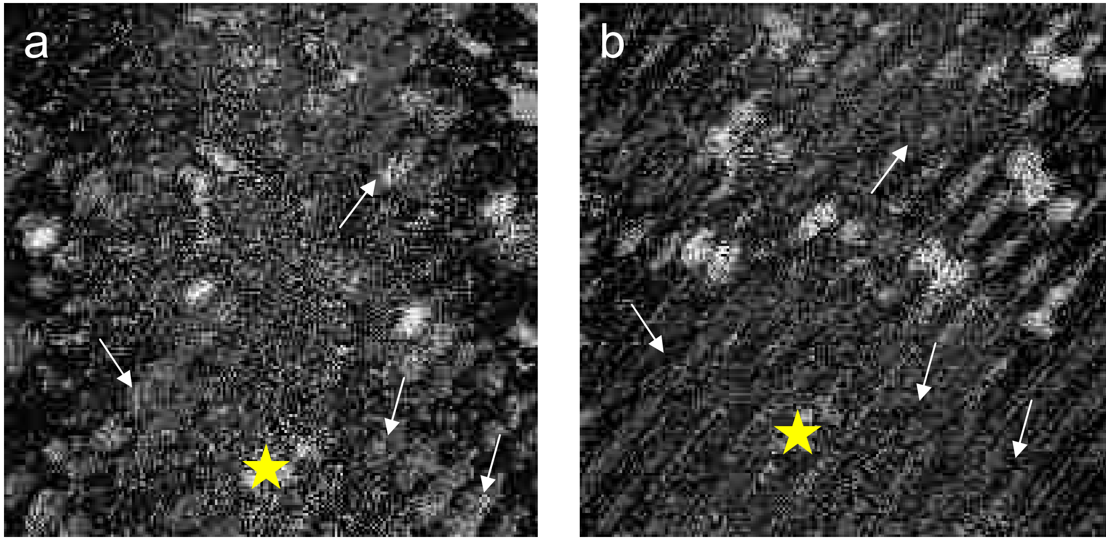

Figure 4-7. Effect of the applied bias magnitude on the resolution of Ge intermixing sites in empty-state STM images. (a) Same image as Figure 4-6(b), low-bias empty-state image at +0.9 V showing locations of Ge incorporation as bright areas. (b) Empty-state image at +1.4 V showing 'pinching off' or 'necking' of Ge intermixing areas, indicated by arrows, caused by delocalization of surface states at high energies. (The yellow star registers a common point between the two images to orient the reader, as a small amount of drift occurred between the two images.)

In addition to the voltage-dependent STM images so far discussed, we now consider the conductance images for the same surface composition of 0.04 ML Ge. The low-bias (+0.8 V) empty-state STM image in Figure 4-8 shows the characteristic dangling-bond (antibonding) states of the surface dimers, along with the individual bright Ge incorporation sites as in Figures 4-6(b) and 4-7(a). The filled-state STM image is low-bias as well (−0.8 V), in which the buckling that is apparent in the empty-state image does not appear. Furthermore, in the filled-state STM image,

bright features (one is pointed to by a white arrow) are seen in the vicinity of the surface defects—possibly due to adsorbates—and appear as dark features in the corresponding filled- and empty-state conductance images.

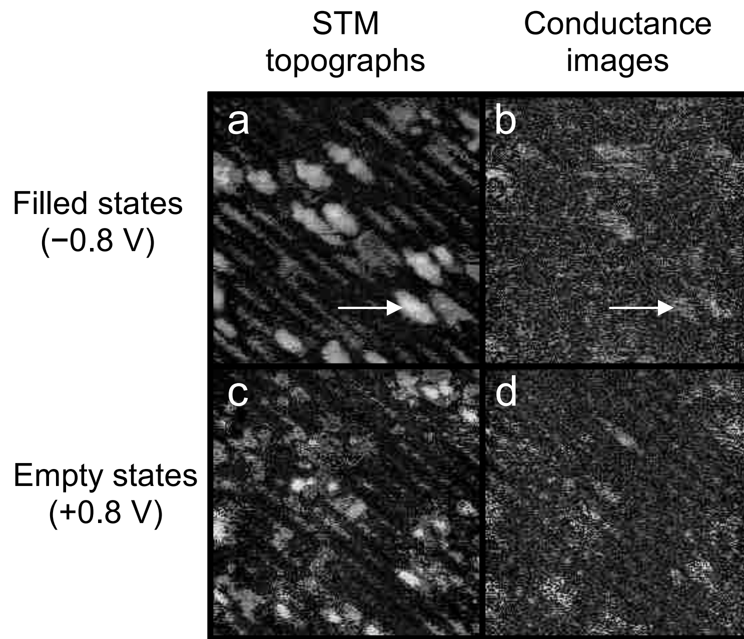

Figure 4-8. SiGe surface with 0.04 ML Ge deposited. (a) Filled-state STM image shows bright features in the vicinity of defects. One example is indicated by white arrow, and appears dark in the filled-state conductance image (b). The empty-state STM image (c) shows the characteristic dangling bonds, which clearly illustrate the buckling of dimers around Ge intermixing sites. (d) The empty-state conductance image show surface defects as dark spots.

The next composition investigated was at 0.10 ML of Ge deposited (Figure 4-9), which appears qualitatively similar to the 0.04 ML Ge surface except with more Ge incorporation sites, as expected. In both the empty-state images [Figures 4-9(b)&(c)], the bright Ge incorporation sites are easily seen. While in the higher voltage image [Figure 4-9(c)], the pinch-off effect described earlier is also apparent (one such occurrence is highlighted with the dotted circle).

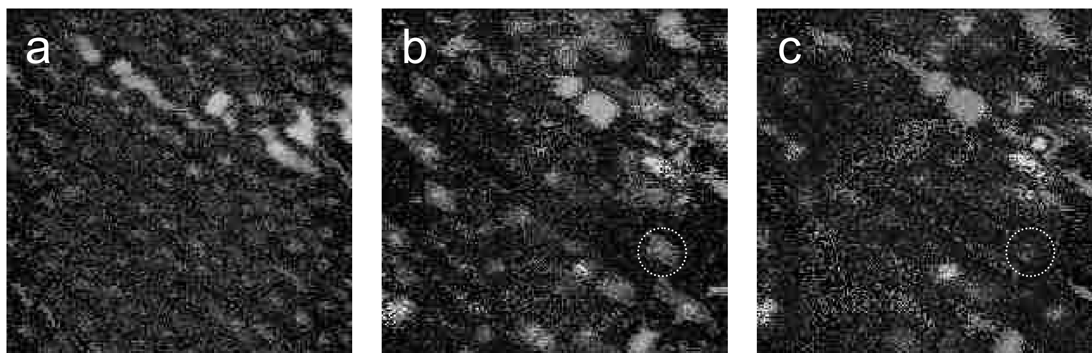

Figure 4-9. Filled- and empty-state STM images of a SiGe surface at 0.10 ML Ge exposure. (a) Filled-state image (−1.1 V) showing a highly buckled surface. (b) Low-bias empty-state image (+1.0 V) showing Ge intermixing sites as bright blurry spots. (c) Empty-state image (+1.1 V) showing the pinch-off effect at the intermix sites. The white dotted circle identifies a region of intermixed Ge.

Upon further Ge exposure to 0.25 ML, the surface is noticeably different in the STM topographs and conductance images as compared to either 0.04 or 0.10 ML of Ge coverage. For instance, in empty-state STM images, instead of isolated bright locations of Ge incorporation; larger, randomly distributed bright and dark domains coexist as shown in Figure 4-10(a). This structuring displays the same spatial distribution in the various images as indicated by the white outlines. However, the contrast in this outlined region is inverted between the empty-state STM image and the corresponding conductance image (akin to a photographic negative). As usual, the empty-state STM image is shifted 90° from the filled-state STM image, such that the dimer rows appear as dark lines; however, these lines are obscured by a considerable amount of delocalization of structure in the form of necking, due to Ge incorporation. The empty-state conductance image, like the empty-state STM image, also shows the dimer rows as black lines, but much better resolved. The filled-state STM image appears normal, with a considerable amount of surface dimer buckling associated with the higher Ge content. The filled-state conductance image shows a grainy, randomly mottled appearance wherein the dimer row structure is absent, and the contrast is inverted from the empty-state conductance image. Finally, the white feature in the lower right

(most likely some unidentified adsorbate) shows as a distinct white spot in the filled-state conductance image, but is absent from the empty-state STM and conductance images.

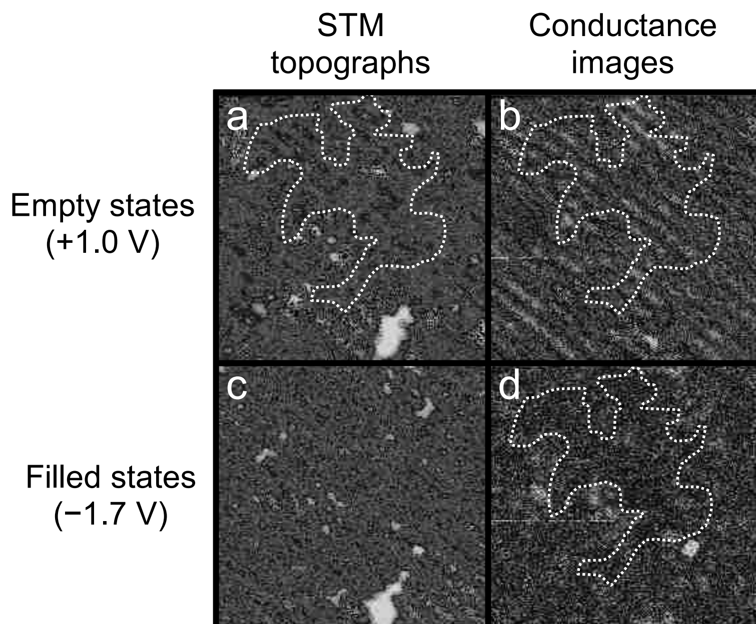

Figure 4-10. SiGe surface at 0.25 ML of Ge. The filled-state STM image (c) shows the surface to be very corrugated with a high degree of buckling. The empty-state STM image (a), shows a random, patchwork of bright and dark regions in which the contrast is reversed from the empty-state conductance image (b). (d) The filled-state conductance image presents a mottled appearance. The bright white dot corresponds to the white blob in (c). The white outline helps to guide the eye.

Figure 4-11 shows the same types of data as Figure 4-10, but at a different location on the surface. The empty-state STM and conductance images appear qualitatively the same as in Figure 4-10, which is expected because the same bias is used (+1.0 V). However, the filled-state STM and conductance images in Figure 4-11 were acquired at a substantially reduced bias magnitude (−1.0 V) as compared to those in Figure 4-10 (−1.7 V), and show noticeable differences. The filled-state STM image shows contrast within the dimer rows—some sections appear brighter than others—whereas in Figure 4-10(c) the dimer rows exhibit a uniform grayscale appearance. Moreover, the conductance image at lower bias magnitude shows much more detailed and

contrasting mottled pattern, appearing almost like “snakeskin” or “fish scales”, with structure apparent along the same direction as the dimer rows and not grainy as in Figure 4-10(d).

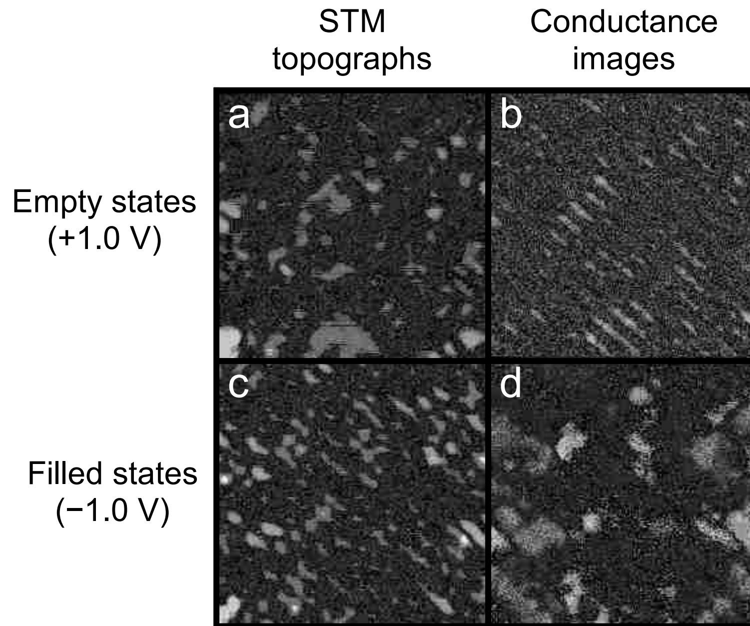

Figure 4-11. SiGe surface at 0.25 ML of Ge. Empty-state STM (a) and conductance images (b) appear qualitatively similar to those in Figure 4-10: mottling with contrast inversion. (c) Low-bias filled-state STM image shows contrasted mottling unlike high bias images. (d) Corresponding conductance image shows a strongly mottled “scalloped” structure.

Figure 4-12 compares filled-state STM and conductance images at two different biases (−1.2 V and −0.9 V) for the same surface area as in Figure 4-11. The −1.2 V STM image shows only subtle variation in contrast of the dimer rows, whereas the −0.9 V image shows this contrast much more strongly as in Figure 4-11. Thus we again see that image contrast and detail varies in proportion to the magnitude of the bias for filled states. However, comparing the conductance images reveals a much stronger and nonlinear effect. While they both show the pronounced mottling as in Figure 4-11(c), the conductance images are not merely contrast enhanced, they show entirely different structure. Thus, we conclude that the conductance images are much more sensitive to changes in bias magnitude than the corresponding STM images.

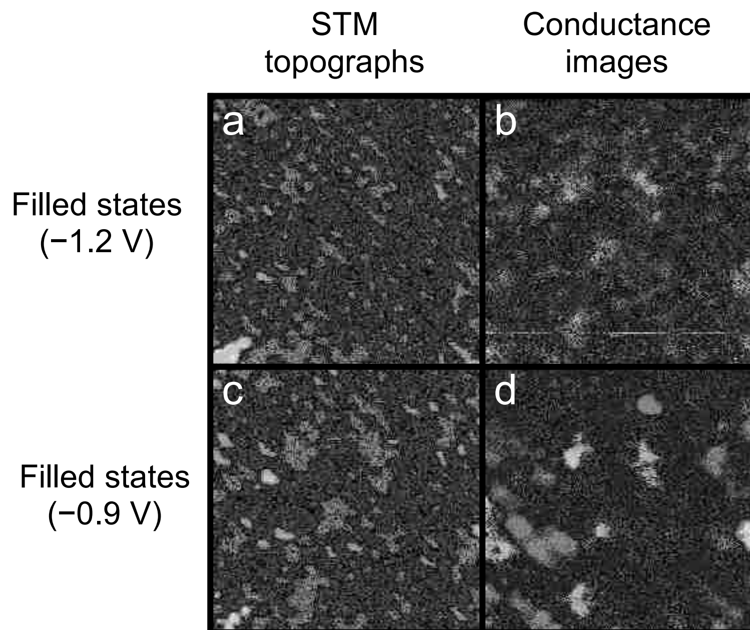

Figure 4-12. SiGe surface at 0.25 ML of Ge. Same surface area as that in Figure 4-11, illustrating the difference in bias magnitude for filled-state STM and conductance images. (a) High-bias filled-state STM image showing buckled surface. (b) High-bias conductance image shows scalloped structure. (c) Low-bias empty-state STM image shows contrast in surface. (d) Low-bias filled-state conductance image shows scalloped structure, but with different features than in the high-bias image, notably the dark spots.

Figure 4-13 shows the same region as in Figure 4-12, but for empty-states (+1.2 V and +0.9 V). The STM topographs display the contrasting, randomly-mottled, bright and dark domains characteristic of Ge intermixing. The conductance images again show the same spatial structuring, contrast inversion (bright to dark), and strong structure corresponding to the dimer rows. Moreover, for the low magnitude bias conductance image [Figure 4-13(d)], structures of bright globules extending along the dimer row direction are apparent.

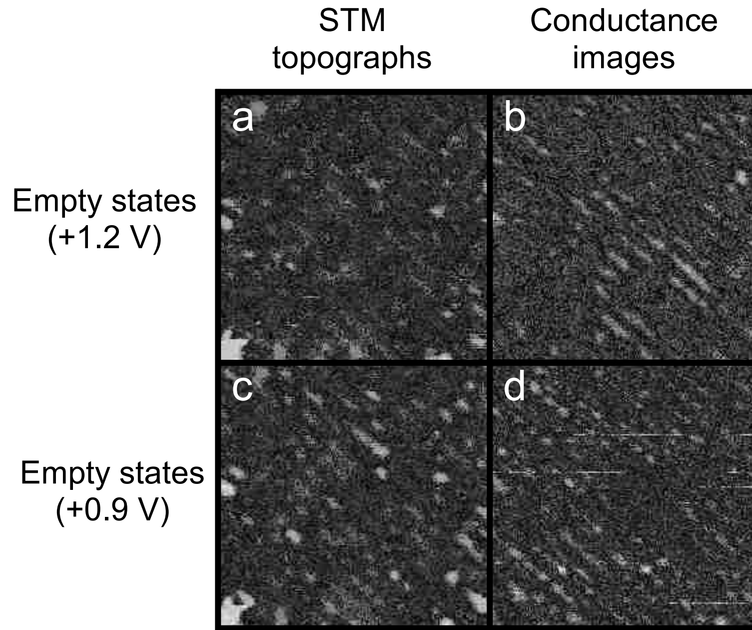

Figure 4-13. SiGe surface at 0.25 ML of Ge. Same area as in Figure 4-12, but empty-state imaging at different bias magnitudes. (a) High-bias empty-state STM image showing large amounts of necking between the dimer rows due to increased Ge composition. (b) High-bias empty-state conductance image showing contrast inversion from (a). (c) Low-bias empty-state image shows Ge intermixing sites as bright puffy areas. (d) Low-bias empty-state conductance image showing strings of bright globules extending along dimer row direction.

Increasing the Ge composition in the alloy even further to 0.5 ML, we begin to see the ordering of defects into short-ranged lines. These weakly ordered dimer vacancy lines (DVLs) indicate the onset of the $2\times n$ reconstruction, and are very irregular, with large values of, and a wide distribution in values for n. In addition to the DVLs, a large proportion of surface dimers are buckled in the $c(4\times2)$ phase, which presents a honeycomb-like appearance in the STM images. Neighboring $c(4\times2)$ domains that are incommensurate are often separated by in phase $p(2\times2)$ buckled borders [9], an example of which is shown in Figure 4-14 by the white arrow.

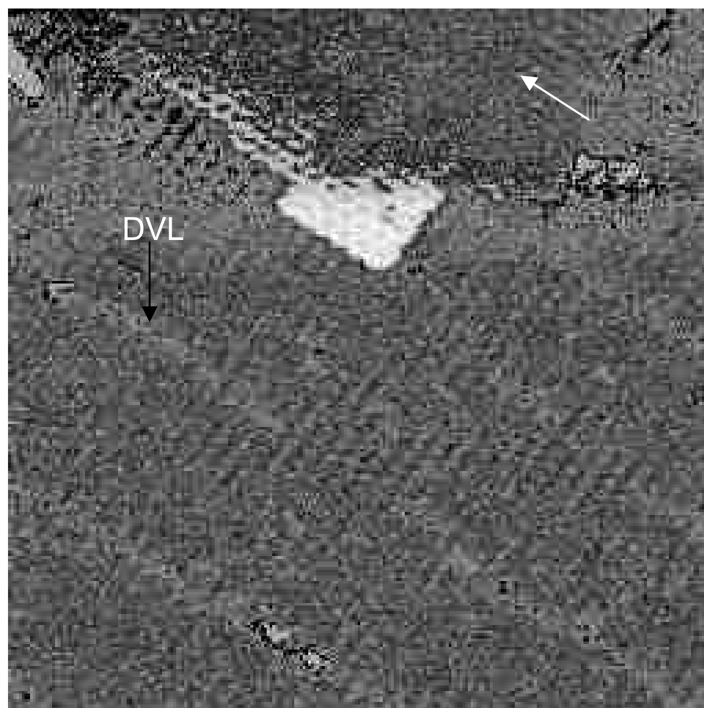

Figure 4-14. Dimer vacancy lines indicating onset of the 2×*n* reconstruction in SiGe alloy. Filled-state STM image of a SiGe surface with 0.5 ML Ge deposited, displaying considerable buckling and formation of weakly-ordered dimer vacancy lines (DVLs). Incommensurate domains of *c*(4×2) are separated by *p*(2×2) borders (white arrow).

Figure 4-15 shows filled- and empty-state STM and conductance images of a SiGe surface at this Ge composition of 0.5 ML. Generally, the images appear qualitatively similar to the 0.25 ML Ge composition surface: highly buckled, surface-mottling, and numerous high contrast domains. However, there is one particularly strong difference: the empty-state conductance image [Figure 4-15(b)], shows the same kind of contrast as filled-state conductance images. This structure is in stark contrast to the type of structure so far seen in empty-state conductance images [Figures 4-10(b), 4-11(b), 4-13(c)-(d)], in which the basic striped dimer row structure is visible as dark lines with domains of contrast. Instead we see snakeskin-like mottled structure typically characteristic of filled-state conductance images. This differing appearance is likely due to the very low applied bias value (+0.4 V), whereas other empty-state conductance images were acquired at higher biases ≥ +0.9 V, and thus may indicate the presence of a surface state at this energy.

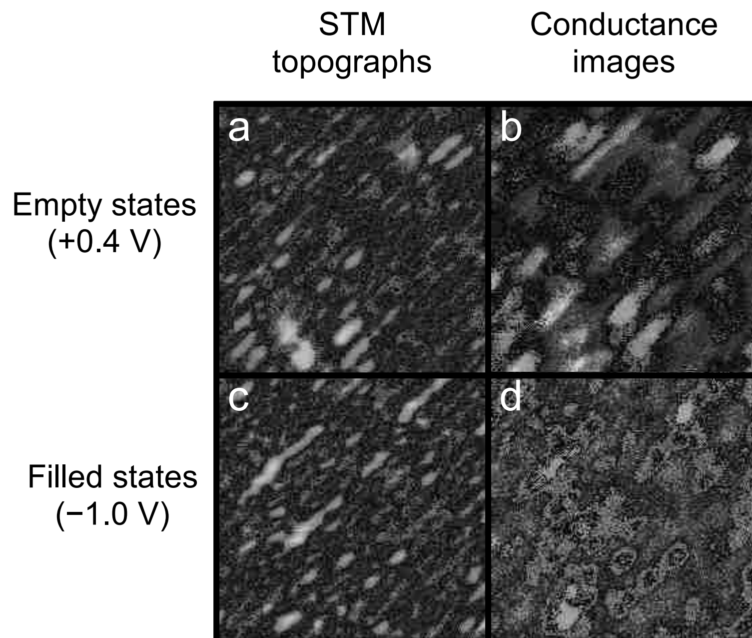

Figure 4-15. SiGe surface at 0.5 ML of Ge. (a) Very low-bias empty-state STM image shows "puffy" dimer rows. (b) Corresponding empty-state conductance image appears qualitatively similar to the filled-state conductance images, in contrast to previous empty-state conductance images likely due to the very low bias magnitude. (c) Filled-state STM image. (d) Filled-state conductance image.

Moreover, another example of the dependence of bias magnitude on conductance images is shown in Figure 4-16, which compares images for two different filled states (−1.9 V and −1.2 V). The low-bias conductance image [Figure 4-16(d)] shows the characteristic snakeskin-like appearance of the surface, but the higher-bias image [Figure 4-16(b)] instead is grainy with little apparent structure. These observations demonstrate the strong dependence of the sensitivity and resolution of conductance images on the magnitude of the bias. This is likely because of the varying density of electronic states at different energies for Si and Ge [18,25]. Knowledge of the distribution of the density of states for Si and Ge can help to focus on the ideal voltage ranges to study SiGe alloy surfaces.

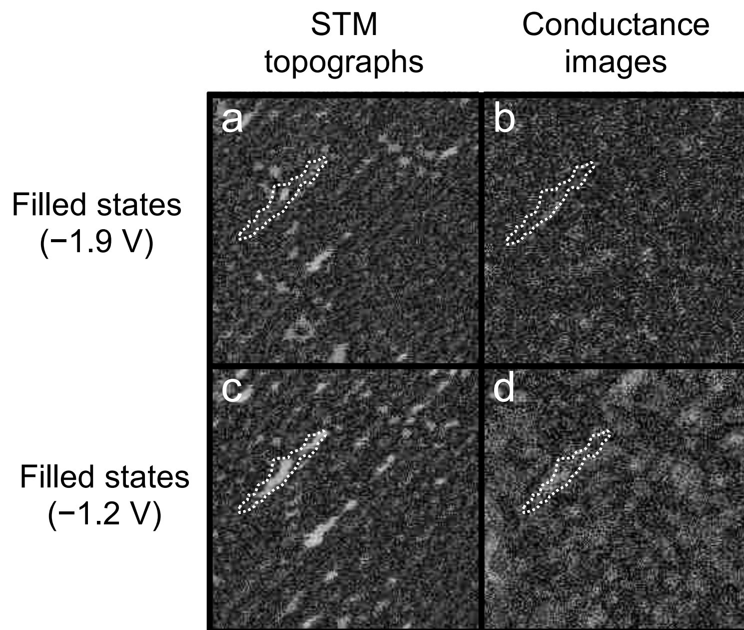

Figure 4-16. SiGe surface at 0.5 ML of Ge. Filled-state images showing effect of bias magnitude. (a) High-bias STM image showing buckling. (b) High-bias conductance image is grainy and fairly featureless. (c) Low bias STM image showing some contrast. (d) Low-bias conductance image showing characteristic contrasting mottled structure. The white dotted outline highlights a common feature in each image and shows the change in contrast.

The final composition investigated is at 1.5 ML of Ge deposited. At this Ge content, the surface forms a well-developed SiGe (2×*n*) wetting layer, typical of those studied in Chapter 3. As shown in Figure 4-17, the 2×*n* reconstruction exhibits periodic, highly-ordered DVLs with *n*~10. Moreover, the surface is extremely corrugated, with most of the dimers exhibiting out-of-phase *c*(4×2) buckling, with in-phase *p*(2×2) borders separating neighboring incommensurate domains. The STM topographs do not display any of the mottled contrast as those at sub-monolayer compositions. However, one particular feature to note is the clear discrepancy between the phases of buckling between the filled- and empty-state STM topographs. The *apparent* buckling of the dimer rows is antisymmetric (white rectangle). Again, this effect is attributed to the aspects discussed above (i.e., charge transfer etc.).

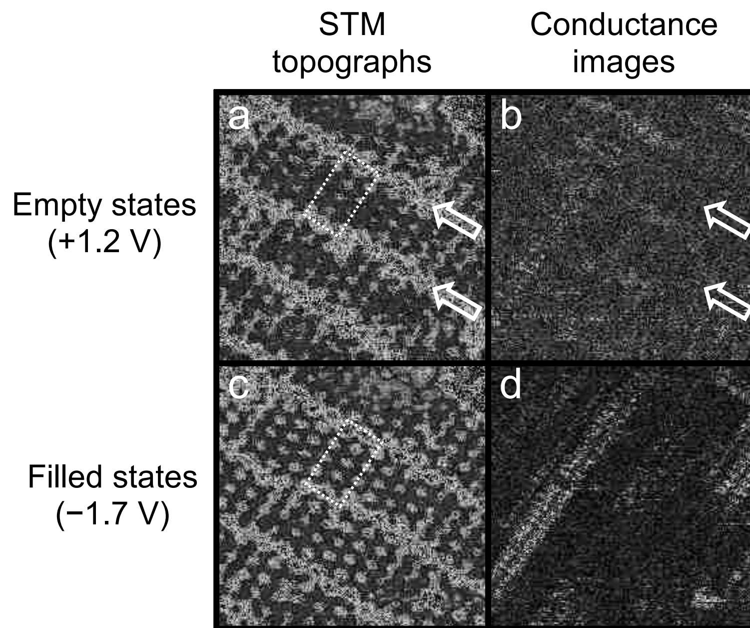

Figure 4-17. SiGe surface at 1.5 ML of Ge. Fully-developed $2 \times n$ wetting layer exhibiting periodic DVLs (white arrows). (a) Empty-state STM image showing extremely buckled $c(4 \times 2)$ surface, which is a mirror image to the buckling in the filled-state STM image (c) (see white dotted rectangle). (b) Empty-state conductance image shows dark bands in the position of the DVLs, but wider in extent (white arrows). (d) Filled-state conductance image is essentially featureless.

Regarding the conductance images of this surface, the rich contrast and detail present in images such as Figures 4-9 and 4-11 is absent. This is interpreted by the fact that Ge tends to wet the Si surface due to its lower surface energy; however, some degree of Si and Ge intermixing is expected, especially at elevated growth temperatures. Calculations [40] indicate that for Ge coverage ~1.5 ML, the surface atomic fraction of Ge is more than 90%. The predominant amount of Ge on the surface at this composition would essentially behave as a pure Ge surface, to first order. Therefore, as for the case of a pure Si(001) surface (Figure 4-5), a lack of detail and contrast in the conductance images might be expected. However, a subtle structure is apparent in the conductance image of Figure 4-17(b): the dimer vacancy lines—which are clearly seen in the STM images (filled and empty)—manifest as dark stripes or bands many times wider in the conductance image.

This observation regarding the appearance of the DVLs is attributed to higher order effects interpreted in light of the work by Nurminen and coworkers [41]. In their simulations of the reconstruction and intermixing of Ge films grown on Si(001), they address the effects of site selectivity that DVLs have on Ge incorporation during growth. They calculated the region beneath DVLs to be unfavorable to Ge incorporation (down to the seventh layer) due to the existence of compressive stresses from the inward relaxation of surrounding atoms at DVLs. This spatially inhomogeneous distribution of Ge and Si might presumably influence the electronic structure at the alloy surface. Thus, areas around the DVLs that are depleted of germanium (Si rich) appear as the dark bands in the conductance image, whereas the Ge rich areas in between are brighter.

4.3 *Conclusions*

The above results of the preliminary STS studies on variable composition SiGe alloy surfaces indicate that differences between Si and Ge, such as size and electronegativity, allow detail in both electronic and physical structure to be observed. For low Ge compositions up to at least 0.10 ML, low-voltage, empty-state STM imaging enables identification of individual Ge intermixing sites. In the range of 0.25–0.5 ML, STS conductance imaging shows considerable contrast and detail, appearing mostly as random mottling. At Ge compositions corresponding to 1.5 ML, a well-developed $2\times n$ reconstruction ($n\sim10$) exists. No distinct structure exists in STS images, and the strong, detailed contrast apparent at lower Ge compositions in the conductance images is greatly diminished. This loss of structure is attributed to the predomination of Ge on the surface at this composition. However, a more subtle effect is apparent in the conductance images: The dimer vacancy lines of the $2\times n$ reconstruction manifest as dark bands much wider in extent than the DVLs themselves, whereas the surface in between the DVLs appears brighter. This effect is believed to

be caused by a spatially inhomogeneous distribution of Ge and Si in the subsurface layers, with Ge concentrated between the DVLs and excluded in their vicinity. In light of these results, resolution of specific atomic ordering of Ge in Si(001) seems to be limited to compositions of less than ~1 ML. For higher Ge compositions, a more global, averaged understanding of the distribution of Ge in the surface is achievable. These results are promising for determining chemical contrast in the SiGe system and warrant more extensive work to be performed. Future experiments might focus on issues such as atomic-resolved STS of low composition Ge in Si(001) to map the electronic structure, STS studies of addimer chain structures on the $2\times n$ surface, as well as investigation of individual C-dimer dynamics and electronic structure using atom-tracking STM/STS [42,43].

4.4 *References*

[1] J. Tersoff, *Appl. Surf. Sci.* **188**, 1 (2002).

[2] M. Schmid and P. Varga, Chapter 4: Segregation and surface chemical ordering–an experimental view on the atomic scale, in *The Chemical Physics of Solid Surfaces, Vol. 10: Surface Alloys and Alloy Surfaces,* (Ed. D.P. Woodruff, Elsevier Science 2002).

[3] C. Nagl, O. Haller, E. Platzgummer, M. Schmid, and P. Varga, *Surf. Sci.* **321**, 237 (1994).

[4] C. Nagl, E. Platzgummer, O. Haller, M. Schmid, and P. Varga, *Surf. Sci.* **331–333**, 831 (1995).

[5] J.A. Appelbaum, G.A. Baraff, and D.R. Hamann, *Phys. Rev. Lett.* **35**, 729 (1975).

[6] D.J. Chadi, *Phys. Rev. Lett.* **43**, 43 (1979).

[7] R.M. Tromp, R.J. Hamers, and J.E. Demuth, *Phys. Rev. Lett.* **55**, 1303 (1985).

[8] R.J. Hamers, R.M. Tromp, and J.E. Demuth, *Phys. Rev. B* **34**, 5343 (1986).

[9] R.A. Wolkow, *Phys. Rev. Lett.* **68**, 2636 (1992).

[10] E. Landemark, C.J. Karlsson, Y.-C. Chao, and R.I.G. Uhrberg, *Phys. Rev. Lett.* **69**, 1588 (1992).

[11] H. Tochihara, T. Amakusa, and M. Iwatsuki, *Phys. Rev. B* **50**, 12262 (1994).

[12] J. Ihm, M.L. Cohen, and D.J. Chadi, *Phys. Rev. B* **21**, 4592 (1980).

[13] F.J. Himpsel and Th. Fauster, *J. Vac. Sci. Technol. A* **2**, 815 (1984).

[14] R.J. Hamers, R.M. Tromp, and J.E. Demuth, *Surf. Sci.* **181**, 346 (1987).

[15] J. Pollmann, P. Krüger, and A. Mazur, *J. Vac. Sci. Technol. B* **5**, 945 (1987).

[16] R.J. Hamers, Ph. Avouris, and F. Bozso, *J. Vac. Sci. Technol. A* **6**, 508 (1988).

[17] R.J. Hamers and U.K. Köhler, *J. Vac. Sci. Technol. A* **7**, 2854 (1989).

[18] J.J. Boland, *Phys. Rev. Lett.* **67**, 1539 (1991).

[19] J. Dabrowski and M. Scheffler, *Appl. Surf. Sci.* **56–58**, 15 (1992).

[20] J.E. Northrup, *Phys. Rev. B* **47**, 10032 (1993).

[21] A.W. Munz, Ch. Ziegler, and W. Göpel, *Phys. Rev. Lett.* **74**, 2244 (1995).

[22] X.R. Qin and M.G. Lagally, *Phys. Rev. B* **59**, 7293 (1999).

[23] K.S. Nakayama, M.M.G. Alemany, T. Sugano, K. Ohmori, H. Kwak, J.R. Chelikowsky, and J.H. Weaver, *Phys. Rev. B* **73**, 035330 (2006).

[24] X.R. Qin, B.S. Swartzentruber, and M.G. Lagally, *Phys. Rev. Lett.* **84**, 4645 (2000).

[25] J.A. Kubby, J.E. Griffith, R.S. Becker, and J.S. Vickers, *Phys. Rev. B* **36**, 6079 (1987).

[26] D.-S. Lin, T. Miller, and T.-C. Chiang, *Phys. Rev. Lett.* **67**, 2187 (1991).

[27] J.E. Rowe and G.K. Wertheim, *Phys. Rev. Lett.* **69**, 550 (1992).

[28] L. Patthey, E.L. Bullock, T. Abukawa, S. Kono, and L.S.O. Johansson, *Phys. Rev. Lett.* **75**, 2538 (1995).

[29] X. Chen, D.K. Saldin, E.L. Bullock, L. Patthey, L.S.O. Johansson, J. Tani, T. Abukawa, and S. Kono, *Phys. Rev. B* **55**, R7319 (1997).

[30] Y.-J. Ko, K.-H. Park, J.S. Ha, and W.S. Yun, *Phys. Rev. B* **60**, 8158 (1999).

[31] S.J. Jenkins and G.P. Srivastava, *Surf. Sci.* **377**, 887 (1997).

[32] R.H. Miwa, *Surf. Sci.* **418**, 55 (1998).

[33] X.R. Qin, F. Liu, B.S. Swartzentruber, and M.G. Lagally, *Phys. Rev. Lett.* **81**, 2288 (1998).

[34] S. Tang and A.J. Freeman, *Phys. Rev. B* **50**, 10941 (1994).

[35] M.T. Yin and M.L. Cohen, *Phys. Rev. B* **24**, 2303 (1981).

[36] M. Tsuda, T. Hoshino, S. Oikawa, and I. Ohdomari, *Phys. Rev. B* **44**, 11241 (1991).

[37] S. Tang, A.J. Freeman, and B. Delley, *Phys. Rev. B* **45**, 1776 (1992).

[38] L. Spiess, A.J. Freeman, and P. Soukiassian, *Phys. Rev. B* **50**, 2249 (1994).

[39] R.M. Feenstra, J.A. Stroscio, J. Tersoff, and A.P. Fein, *Phys. Rev. Lett.* **58**, 1192 (1987).

[40] R.J. Wagner and E. Gulari, *Phys. Rev. B* **69**, 195312 (2004).

[41] L. Nurminen, F. Tavazza, D.P. Landau, A. Kuronen, and K. Kaski, *Phys. Rev. B* **68**, 085326 (2003).

[42] B.S. Swartzentruber, *Phys. Rev. Lett.* **76**, 459 (1996).

[43] X.R. Qin, B.S. Swartzentruber, and M.G. Lagally, *Phys. Rev. Lett.* **85**, 3660 (2000).

Chapter 5

Conclusions and future directions

The purpose of this Thesis was to investigate the surface processes that occur on the SiGe wetting layer during Ge epitaxy on the technologically-important Si(001) surface. A detailed understanding of the surface processes, the dominant mass transport species, and kinetics at the atomic scale enables potentially greater control during growth to increase the qualities of grown films and nanostructures. Toward this end, a series of investigations using scanning tunneling microscopy/spectroscopy was conducted.

We have discovered that the predominant mass transport species on the Ge-Si(001)–(2×*n*) wetting layer are so-called *addimer chain structures* (ADCSs). ADCSs are composed of type-C dimers that reside in the troughs between dimer rows extending along all equivalent ⟨130⟩ directions of the surface, giving rise to a zigzagged morphology. ADCSs are metastable, as evidenced by their transition to compact epitaxial islands (CEIs), which are segments of the next epilayer. Because the transition of ADCSs to CEIs is a thermally-activated process, we determined the associated activation energy E_a and prefactor ν_0. These kinetic values were determined by a series of experiments that monitored the populations of ADCSs as they transitioned to CEIs as a function of time for five temperatures (90, 120, 130, 140, and 150 °C). The exponential decay of the ADCS populations displays an associated characteristic decay time at each temperature. By analyzing the rates of decay as a function of temperature according to an Arrhenius-type expression, we computed the activation energy as $\sim 0.7 \pm 0.2$ eV with an associated prefactor of $\sim 5\times10^{4\pm2}$ s^{-1}. While the value for the activation energy is low compared to most diffusion-related surface phenomena involving dimers (of the order of ~1eV), the prefactor is *anomalously* low, by about 10

orders of magnitude. We speculate that this low value may reflect the possibly complicated nature of the conversion mechanism, which is likely a multi-bodied, substrate-strain-mediated concerted rearrangement of the ADCS dimers with the substrate dimers. Our speculation is based on observations that ADCSs exhibit extremely localized movement while preserving their chain-like structure; and upon movement, a concomitant motion of the surface dimer structure is observed. *Thus an interesting direction for future research might focus on the origin of the anomalously low prefactor, perhaps as it relates to the proposed transition mechanism. Future research might also focus on more detailed STM studies at cryogenic temperatures to observe ADCSs form from adatoms to test the validity of the proposed Adatom-Trapping-Addition formation mechanism. Such information could be used in conjunction with more detailed studies of the transition of ADCSs to CEIs to provide details for advanced molecular dynamics or ab initio simulations.*

Because ADCSs are the predominant mass transport species on the SiGe $2\times n$ surface near room temperature, a series of preliminary tunneling spectroscopy investigations was performed to determine the structure of this surface, with the main objective of achieving chemical contrast between Si and Ge. Two spectroscopic techniques were used: voltage-dependent STM and scanning tunneling spectroscopy. A number of surfaces were studied with progressively increasing Ge composition, so that any changes could be observed and associated to Ge content. The results of these studies identified Ge intermixing sites in the Si(001) surface for low Ge compositions, less than ~0.10 ML. At higher surface compositions, conductance images and voltage-dependent STM images displayed structure and contrast in the surface, mostly as randomized mottling. The results suggest that achieving chemical contrast in this system is certainly possible. *Future work might focus on a more detailed mapping of the structure of SiGe alloy surfaces with atomic resolution, especially in conjunction with the presence of ADCSs. Another interesting direction would be to perform atom-tracking*

tunneling spectroscopy of ADCSs as they convert to epitaxial islands to observe changes in electronic structure associated with the transition.

A final area of interest for future work involves the demonstration of large-area low defect density epitaxial Ge films grown on Si(001) substrates [1–3]. The technique relies on the selective growth of Ge on Si over SiO_2 when Ge is deposited on very thinly oxidized Si(001). The proposed mechanism involves the presence of all three species (Ge, Si, and SiO_2) and the formation of volatile species. Certainly an atomic-level understanding of the details of this process can help to better control this technique. *Future work could possibly focus on observing and/or initiating a tri-molecular reaction between these species on a noble metal surface (again probably performed at cryogenic temperatures to isolate and manipulate individual species). Another approach is to selectively oxidize certain regions of a Si(001) substrate such that Si and SiO_2 are both present. Subsequent Ge deposition on this biphasic surface should yield interesting possibilities for experiments.*

5.1 *References*

[1] Q. Li, S.M. Han, S.R.J. Brueck, S. Hersee, Y.-B. Jiang, and H. Xu, *Appl. Phys. Lett.* **83**, 5032 (2003).

[2] Q. Li, Y.-B. Jiang, H. Xu, S. Hersee, and S.M. Han, *Appl. Phys. Lett.* **85**, 1928 (2004).

[3] Q. Li, J.L. Krauss, S. Hersee, and S.M. Han, *J. Phys. Chem. C* **111**, 779 (2007).

Appendix

Image processing algorithm*

*Prof. Lance Williams (UNM Computer Science) is gratefully acknowledged for his work in developing the following image processing routine used to extract data from STM images.

There is a small lateral shift between corresponding filled- and empty-state images due to piezoelectric tube hysteresis, so the images are first registered via maximization of mutual information. Next, the empty-state images are bandpass filtered by convolving with a Laplacian of Gaussian. The purpose of this is twofold: (*i*) By differentiating the image twice, the dc component of the Fourier transform is removed, which has the effect of negating the height difference between neighboring terraces in the image. (*ii*) The standard deviation of the Laplacian of Gaussian is set approximately the same as the radius of atoms (2 pixels) to serve as a matched filter. This enhances the contrast of the adspecies (ADCSs and compact islands) compared to the background (surface). Third, a mask is created to suppress false positive responses at plateau boundaries (i.e., step edges). This is accomplished by thresholding the gradient magnitude of filled- and empty-state images. Fourth, morphological close and open operations are then applied to remove small regions from the binary image representing the product of the thresholded, bandpass-filtered image and the mask.

The above operations result in binary images of filled- and empty-states, in which only ADCSs and compact islands are isolated, while the effects of differing plateau heights, false responses at step edges, and noise are removed. A classification procedure is finally performed to discriminate between ADCSs and compact epitaxial islands. Both filled- and empty-state images are used

because ADCSs only appear in empty-state images. First, a bounding-box is created for all ADCSs and compact islands in empty-state images. Next, the centers-of-mass are computed for compact islands in filled-state images. Two criteria are imposed to distinguish ADCSs from compact islands: (i) If the center-of-mass of an object in filled-state images lies within a corresponding bounding box in empty-state images; *and* (ii) if there is no more than a factor-of-two difference in size, the feature is verified positively as a compact island. If these criteria are not met, the object is identified as an ADCS.

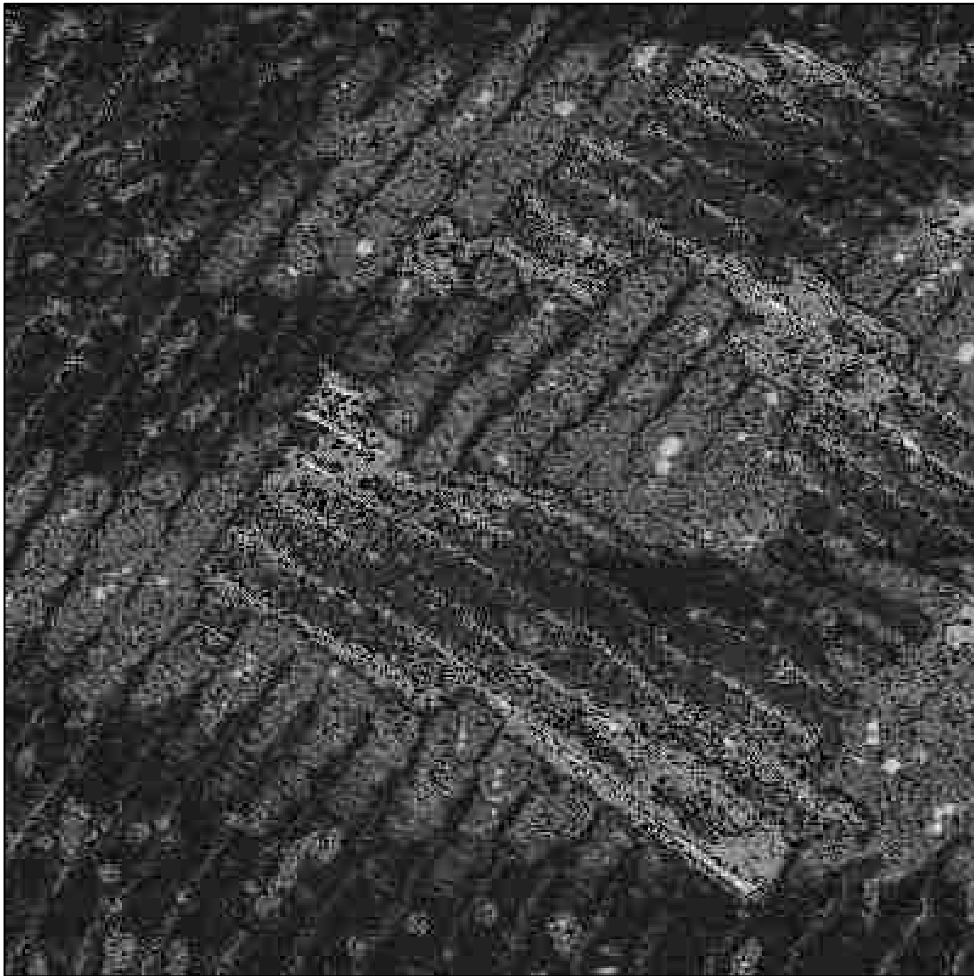

Figure A-1. Original empty-state STM image. A typical large-area scan (500 Å × 500 Å) showing multiple terraces of the SiGe 2×*n* surface and adspecies (ADCSs and compact islands).

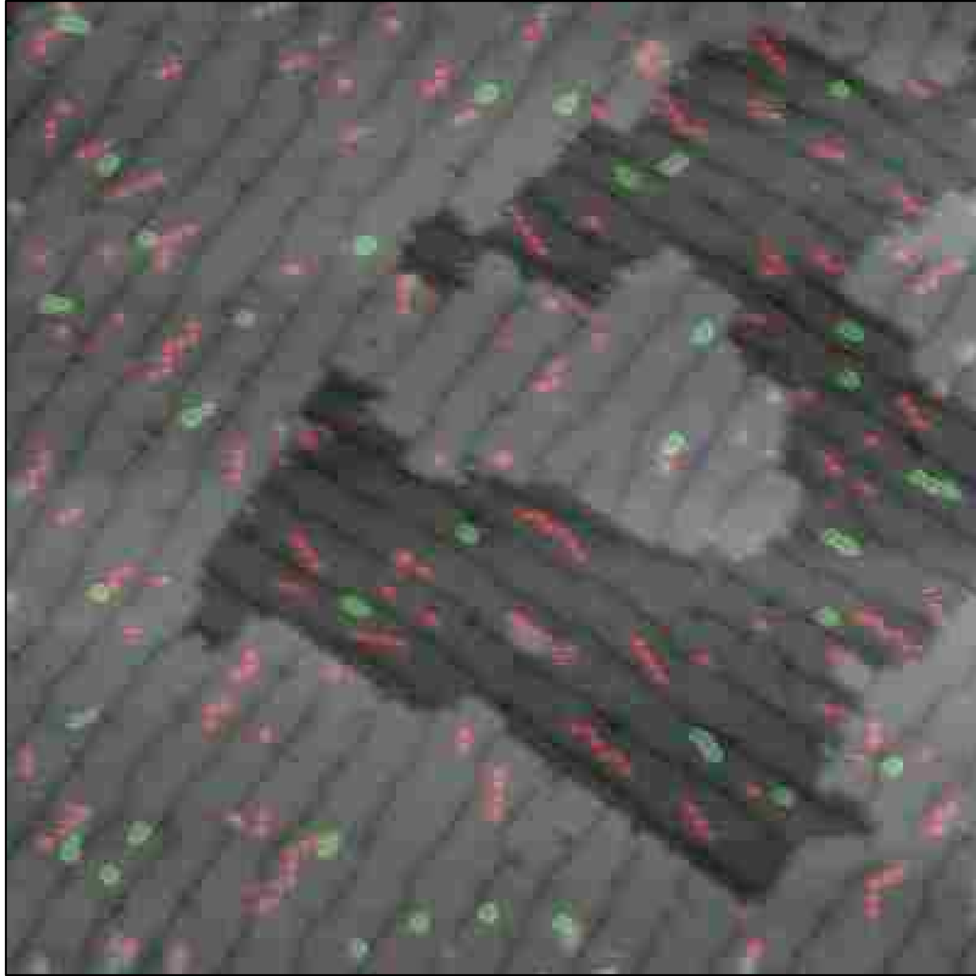

Figure A-2. Processed empty-state STM image. After the image processing algorithm is applied to the image, the ADCSs are highlighted in red and the compact islands are in green. While there are some misclassifications, the algorithm is generally quite robust. The areas in pixels of each type of adspecies are extracted from such images and used to monitor the populations over time.